Title

An Autonomous 3D Biofluid Management and Analysis Lab-on-the-Body Platform for Point-of-Person Biomarker Monitoring Applications

Author

Lin, Haisong

Publication Date

2019

Peer reviewed|Thesis/dissertation

UNIVERSITY OF CALIFORNIA

Los Angeles

An Autonomous 3D Biofluid Management and Analysis Lab-on-the-Body Platform for Point-of-Person Biomarker Monitoring Applications

A thesis submitted in partial satisfaction

of requirements for the degree Master of Science

in Electrical Engineering

by

Haisong Lin

2019

ABSTRACT OF THE THESIS

An Autonomous 3D Biofluid Management and Analysis Lab-on-the-Body Platform for Point-of-Person Biomarker Monitoring Applications

by

Haisong Lin

Master of Science in Electrical Engineering

University of California, Los Angeles, 2019

Professor Sam Emaminejad, Chair

Personal biomarker sensors are poised to transform personalized medicine by providing frequent and real-time measures of biomarker molecules, thus catalyzing the transition from point-of-lab and point-of-care testing to near-continuous monitoring at the point-of-person. To realize the full range of possibilities offered by such wearable and mobile sensors, *in-situ* active microfluid management capabilities are fundamentally required. Previously reported non-invasive wearable and mobile biomarker sensors rely on the *in-situ* analysis of biofluid samples that are passively collected in absorbent pads or 2D microfluidic housings. The spatial constraints of these platforms and their lack of active control on biofluid inherently limit the efficiency, diversity and frequency of end-point assessments. Here, by devising a suite of programmable electro-fluidic interfaces, integrated within a multi-layer flexible microfluidic device, we demonstrate key biofluid management functionalities, including biofluid flow actuation and compartmentalization, for autonomous lab-on-the-body sample analysis. System-level functionality is achieved by

interfacing the microfluidic device with a wireless circuit board. The desired operations are validated on-body through human subject testing. The versatility of these unprecedented lab-on-the-body methodologies enables a wide-ranging complex sample processing and analysis operations that can converge to realize point-of-person monitoring platforms.

The thesis of Haisong Lin is approved.

Dino Di Carlo

Robert N. Candler

Sam Emaminejad, Committee Chair

University of California, Los Angeles

2019

TABLE OF CONTENTS

LIST OF FIGURES

ACKNOWLEDGEMENTS

First, I would like to express my sincere gratitude to my advisor, Professor Sam Emaminejad, for his passion and wisdom that inspired me about this work and for his professional and patient guidance that helped me to finish this work.

I would like to appreciate Professor Dino Di Carlo and Professor Robert N. Candler for serving as my thesis committee members and offering me their insightful comments.

I would also like to thank my colleagues: Yichao, Hannaeh, Shuyu, Bo, Xuanbing, Zhaoqing, Jiawei, Wenzhuo and Christopher from the Interconnected & Integrated Bioelectronics Lab for their great contribution and generous feedback for this work . I really love the family-like environment of our lab and productive collaboration with them.

Finally, I would like to thank my family and my girlfriend, Xingyu, for their unconditional love and support.

Chapter 1 Introduction

1.1 Background of wearable biosensing system

Personal biomonitoring technologies enable personalized and precision medicine, as they allow for the longitudinal and objective assessment of the health status of individuals in real-time. Currently, the majority of commercialized non-invasive health monitoring sensors are only capable of tracking physical activities and vital signs, and they fail to access molecular-level biomarker information that provide insight into our body's dynamic chemistry [1-10]. In that regard, a new class of wearable and mobile personal monitoring technologies are needed to track biomarkers by non-invasively sampling, processing and analyzing biofluids, as rich reservoirs of biomarkers [11,12] (Fig 1.1). The development and deployment of such technologies would create an unprecedented era of personalized medicine as they catalyze the transition from point-of-lab and point-of-care testing (with sparse sampling intervals on the order of months and years) to near-continuous point-of-person monitoring (with sampling intervals on the order of minutes and hours) [13-19].

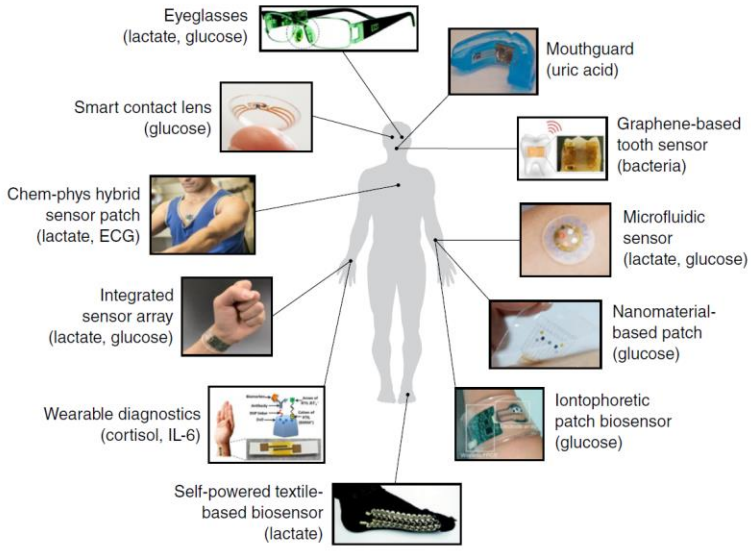

Figure 1.1: Representative examples of noninvasive biosensing system [12].

Recent advances in electrochemical sensor development, flexible and microfluidic device fabrication, and low power electronics have now set forth a path toward implementing miniaturized and lab-on-the-body-like platforms dedicated to biofluid sample processing and analysis at the point-of-person. Previously reported wearable and mobile biomarker sensors successfully demonstrated electrochemical and colorimetric sensing interfaces for detection of analytes in micro- to millimolar ranges and in a sample-to-answer manner. These sensors rely on the analysis of biofluid samples that are passively collected in absorbent pads [20-22] or 2D microfluidic housings [23-25] (Fig 1.2). Accordingly, their analytical operations are limited due to the lack of active control on the biofluid flow and storage. Therefore, the existing solutions are systematically unable to implement a broad range of critical auxiliary operations (*e.g.*, uncontaminated periodic sampling and sample processing) and to adapt transduction mechanisms that were previously demonstrated in the context of benchtop sensors. To address these shortcomings and to realize a fully autonomous lab-on-the-body platform, fundamentally, *in-situ* biofluid management methodologies must be employed in conjunction with the demonstrated sensing capabilities.

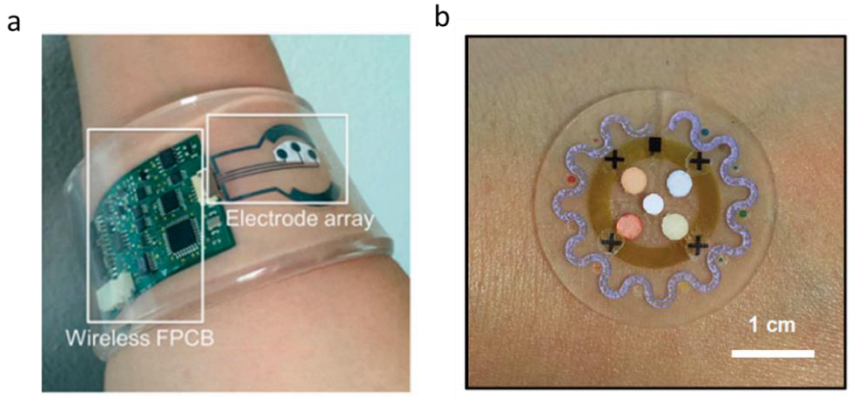

Figure 1.2: Example of sweat sample collection method: (a) absorbent pad [20]. (b) 2D microfluidic housing [23].

1.2 Overview of the lab-on-the-body platform modules

Here, a suite of programmable electro-fluidic interfaces, integrated within a multi-layer flexible microfluidic module, is devised to demonstrate key biofluid management functionalities, including biofluid flow actuation and compartmentalization, for autonomous lab-on-the-body operations. The microfluidic module is created by stacking thin layers of adhesive plastic substrates, patterned with an actuation and sensing electrode array and pre-defined microfluidic embodiments to form channels, vias, and valves. The 3D device architecture enables the implementation of a diverse set of operations in a compact form. To achieve autonomous biofluid actuation and sensing with system-level operation, the microfluidic module is interfaced with a miniaturized and wireless printed circuit board (PCB). The data and control commands are bidirectionally relayed via Bluetooth communication with a custom-developed mobile application.

Electro-fluidic flow actuation has been shown to provide automatable capabilities in terms of controlling the fluid flow, sample processing, as well as enhancing the sensor performance in the context of the lab-on-the-chip devices [26-33]. To adapt the electro-fluidic flow actuation principle for lab-on-the-body applications, we exploit alternating current electrothermal (ACET) flow-based phenomena, which are suitable for the manipulation (*e.g.*, pumping and mixing) of microfluids with high conductivity (*e.g.*, biofluids) [34-37]. Electro-fluidic nature of this actuation method eliminates the need for conventional bulky mechanical pumps, while enabling addressable, programmable and precise microfluid actuation by controlling the applied voltage levels. Alternative electro-fluidic flow actuation techniques such as AC electroosmosis (ACEO) and electrowetting-on-dielectric (EWOD) may not be suitable for wearable applications due to their requirements for low-conductive fluids and relatively high voltage levels [37]. ACET arises in presence of a non-uniform electric field, which establishes temperature gradients and subsequently

local permittivity and conductivity gradients within the fluid, leading to an induced motion of fluids. Here, with proper symmetric and asymmetric designs of electrode configurations, we demonstrated and characterized ACET actuation, through visualizable pumping and mixing phenomena, which are also useful standalone microfluidic operations.

Biofluid sample compartmentalization for lab-on-the-body applications is useful for a variety of purposes. For example, in the context of autonomous periodic iontophoretically-induced sweat analysis, the intermittently induced fresh sweat samples must be analyzed in their designated compartments and in isolation from previous samples to prevent sensor/sample contamination, practically requiring programmable and on-demand compartmentalization operation. To realize biofluid compartmentalization, we devise a wearable valving method, where microfluidic flow is permitted/blocked reversibly, through shrinkage/expansion of a hydrogel. In this way, we are able to overcome the limitations of conventional active valves, which require bulky components and external control equipment, preventing their use from lab-on-the-body applications. The valve is comprised of a thermal-stimuli-responsive hydrogel (embedded in the microfluidic channel) [38-42] and a programmable microheater (patterned on the bottom of the channel). To adapt the valving capability for sampling, routing, and compartmentalizing sweat, directly harvested from high-pressure secreting glands, a pressure release mechanism is devised, motivated by an electronic-hydraulic analogy.

1.3 Integration and clinical utility

By integrating the demonstrated electro-fluidic interfaces with electrochemical sensing surfaces, new degrees of freedom are presented for performing autonomous biomarker sensing-related operations, including temporal sampling, multi-on-demand biomarker sensing, and enhancement

of sensor performance (in the context of amperometric sensing interfaces. The intended biofluid management and sensing operations are validated through a combination of simulation, *in-vitro* characterization, and on-body human subject testing. Our biofluid actuation characterization results follow the same trends as that predicted by electrothermal theory and simulation. In order to illustrate the utility of our technology for the envisioned point-of-person monitoring applications, our actuation-enabled sensors are used to analyze sweat glucose samples. Our sensor readouts successfully tracked the distinct biomarker patterns observed in clinical settings and psychophysiological studies (*e.g.*, elevation of sweat glucose after glucose intake in fasting subjects).

Overall, our results demonstrate the promising potential of the devised methodologies to perform complex sample management and analysis operations, ultimately realizing a fully autonomous lab-on-the-body platform for a broad range of health and wellness monitoring at the point-of-person.

Chapter 2 3D microfluidic architecture and system-level integration

2.1 3D wearable microfluidic design

The 3D microfluidic actuation and sensing wearable technology presented here delivers a suite of programmable biofluid management and electrochemical analysis operations within a compact and flexible architecture. A representative 3D microfluidic-integrated illustration of the actuation and sensing interfaces rendered by our technology is shown in Fig 2.1 to visualize their corresponding individual operations.

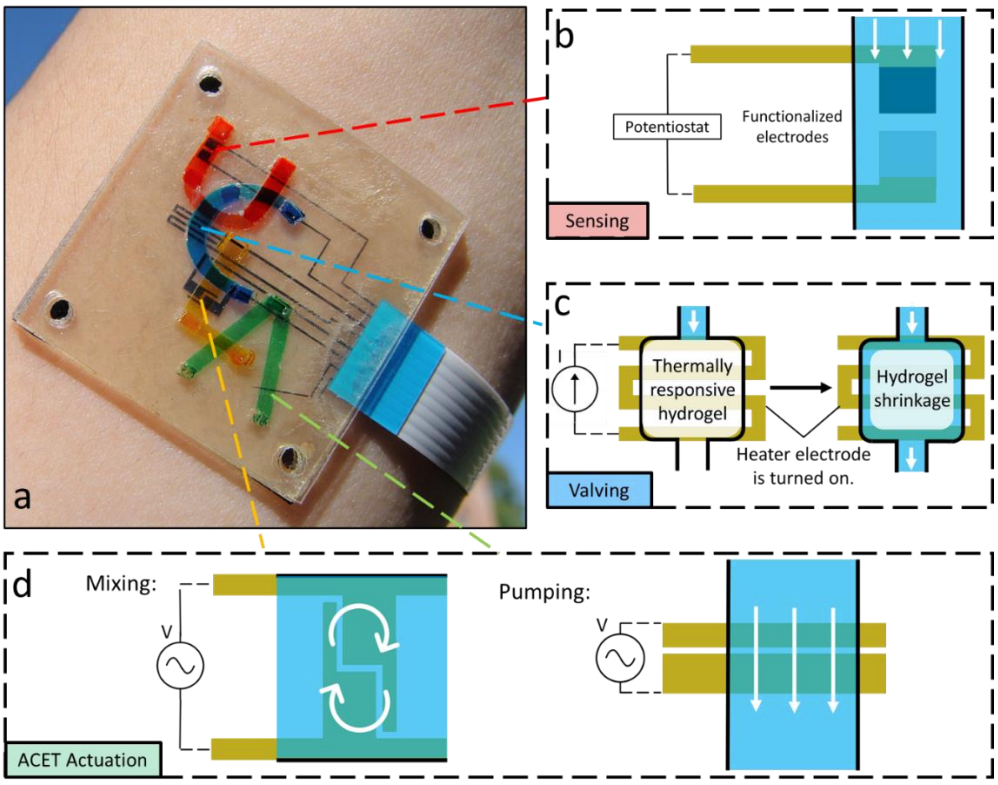

Figure 2.1: (a) A representative design of an actuation and sensing array, embedded within a multi-layer microfluidic module, visualizing (b) electrochemical sensing, (c) valving and (d) biofluid ACET actuation (pumping and mixing).

To achieve functional operations, the substrate layers can be selectively patterned, with actuation and sensing electrodes, as well as chemicals and reagents to implement the intended assays. Electrode pair configurations with various designs are used to implement ACET-induced flows with versatile flow profiles. Thermal-stimuli-responsive hydrogel is incorporated in a microchannel with a serpentine-shaped microheater electrode underneath for valving. The electrochemically functionalized electrode pair is used for sensing of target analytes (Fig. 2.1).

2.2 Wearable microfluidic module fabrication and assembly

The core of the platform is a multi-layer and thin microfluidic module. The microfluidic module was created by assembling several layers of double-sided tape (170 µm-thick, 9474LE 300LSE, 3M) as well as transparent polyethylene terephthalate (PET) film sheet (100 µm-thick, MG Chemicals) which were patterned with actuation and sensing electrodes (Fig. 2.2) .

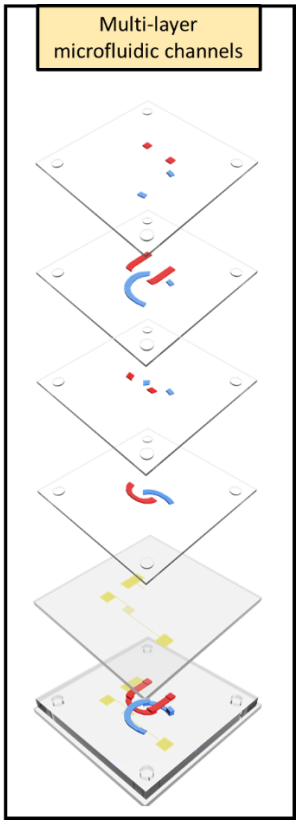

Figure 2.2: Assembly process of the microfluidic module.

The microfluidic embodiments, including microchannels and vias, were created by laser-cutting (Epilog Mini 24, Epilog Laser) 2D patterns within the tape- and the PET-based substrates. With the proper alignment of vias and microchannels, fluidic connections in z-direction were achieved, rendering complex 3D microfluidic structures (Fig. 2.3). The vertical vias connect microchannels from different layers, to implement complex and spatially efficient 3D architectures. For example, as shown in Fig. 2.1a and Fig. 2.3, the red-dyed biofluid in the U-shaped channel goes both over and under the blue-dyed biofluid in the C-shaped channel, while the two liquids are physically isolated.

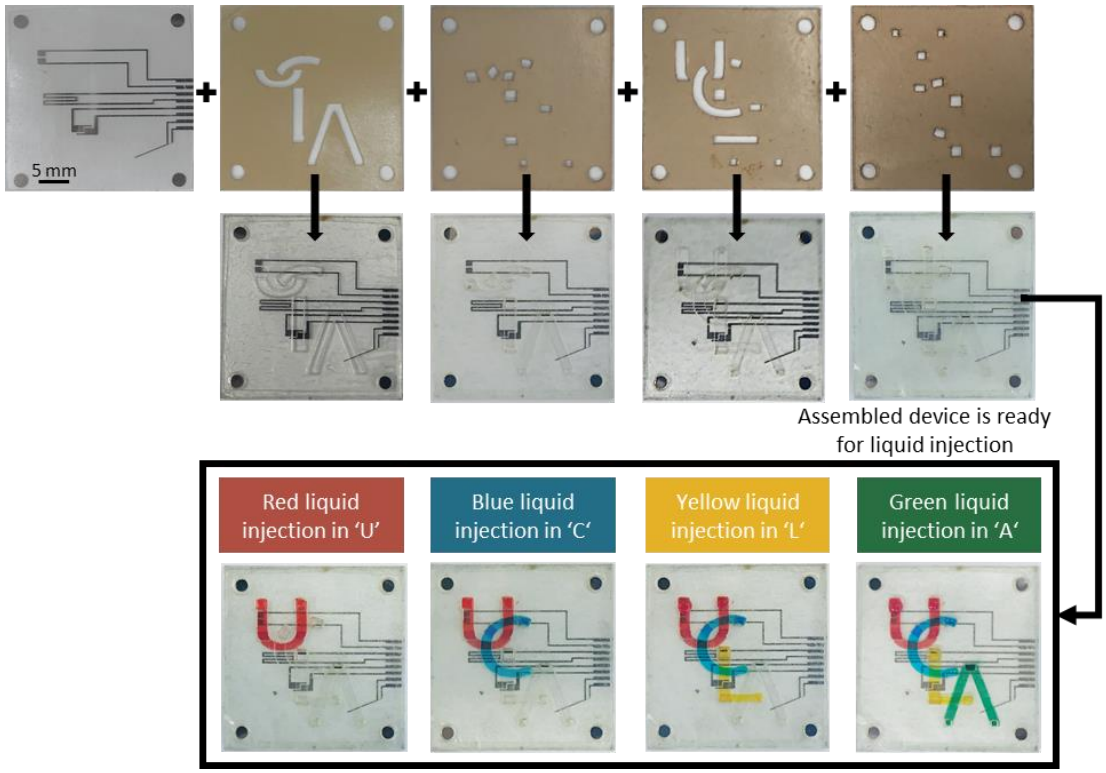

Figure 2.3: Assembly of a representative flexible electronic microfluidic module. Several 2D laser-cut double sided adhesive tapes and PET layers are stacked on top of a multi-functional electrode array (patterned on PET). Green-, Red-, Blue-, and Yellow- dyed artificial sweat samples are

injected in U-, C-, L-, and A-shaped microfluidic channels to visualize this 3D integrated microfluidic module.

As shown in Supplementary Fig. 2.4, the electrode array on PET was patterned by photolithography using positive photoresist (MicroChemicals AZ5214E), followed by evaporation of 20 nm Cr, 100 nm Au, and 20 nm Ti for actuation electrodes and 20 nm Cr and 100 nm Au for sensing electrodes. The lift-off step was performed in acetone.

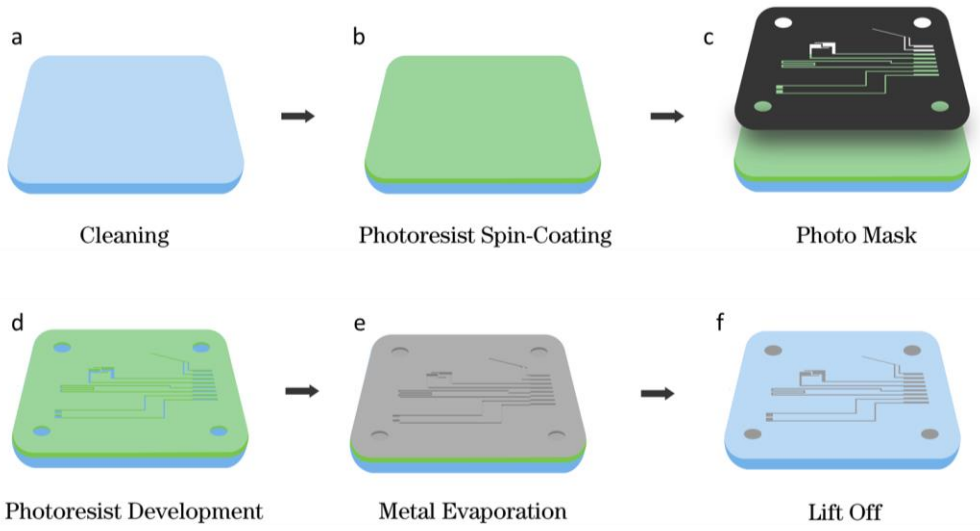

Figure 2.4: The electrode array fabrication. The electrode array is fabricated by the process of: a) cleaning, b) AZ-5214 positive photoresist spin-coating, c) photolithography with the designed mask, d) photoresist development, e) metal evaporation of 20 nm Cr/100 nm Au/20 nm Ti, and f) lift-off in acetone.

2.3 System-level integration

To achieve system-level functionality, the microfluidic module can be interfaced with the PCB using a flexible flat cable and vertically conductive adhesive tapes (Fig. 2.5). The PCB

consolidates the analog and digital integrated circuit chips and peripheral electronics to seamlessly implement the required operations. At its core, the PCB utilizes a microcontroller that can be programmed to control the actuation circuitries and relay the received data from the sensing circuitry via bidirectional Bluetooth communication with a mobile application (Fig. 2. 6).

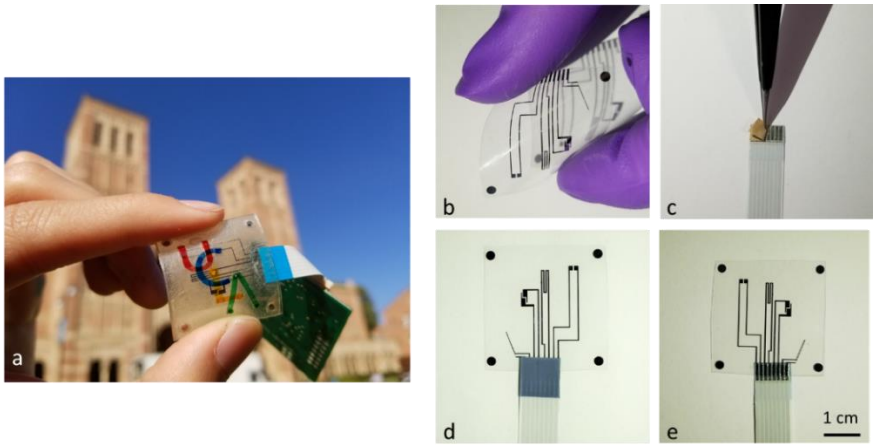

Figure 2.5: (a) Connection of the flexible microfluidic and PCB modules with a flexible cable. (b-d) Establishing electrical connection with a representative sensor and actuator electrode array. (b) Photo of the electrode array patterned on a flexible PET substrate. (c) Placement of a vertically conductive tape on the flexible cable's connection pins. d,e) Front and back views of the assembled cable and the electrode array.

To drive the ACET electrodes, an AC voltage excitation signal was used (in MHz range), and to activate the heater, effectively, a DC source was implemented. Additionally, an illustrative analog signal conditioning circuitry was implemented for sensor output acquisition and noise and interference mitigation. The entire system can be powered by a single miniaturized rechargeable lithium-ion polymer battery with a nominal voltage of 3.7 V.

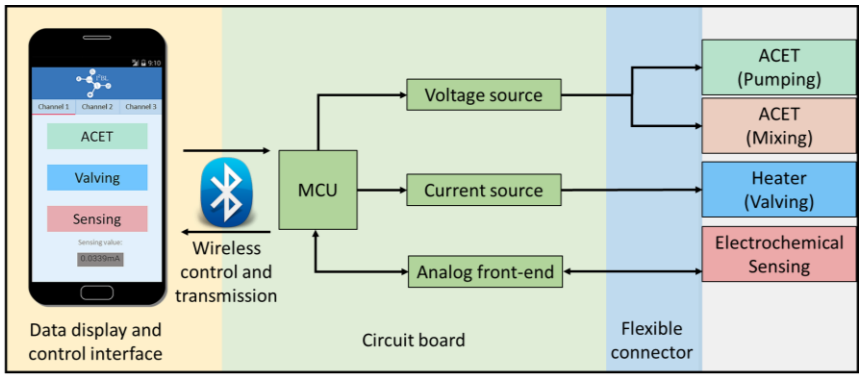

Figure 2.6: System-level block diagram of the PCB module, implementing excitation circuitries (for actuation), signal conditioning circuitries (for sensing), and bilateral data and command communication with a mobile application.

The PCB-controlled microfluidic module, because of its vertical integration methodology, allows for the enhancement of the diversity of the microfluidic operations through the attachment of various microfluidic plugins, while rendering spatially efficient implementations. For example, an adhesive epidermal interfacing collection chamber can be attached underneath the microfluidic module for *in-situ* sweat sampling (Fig. 2.7).

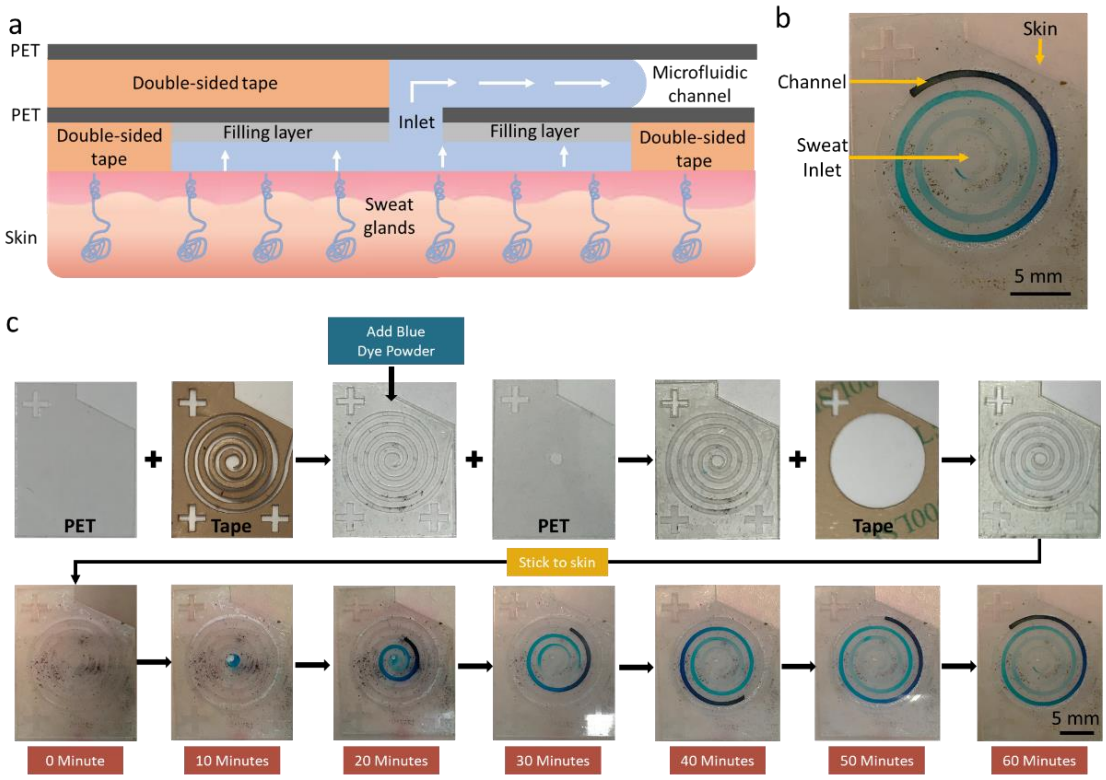

Figure 2.7: (a-b) Microfluidic plugins for sweat collection. Embedded blue dyes (Flavors and color) are used to visualize the liquid path. (c) The sweat collector assembly and sweat collection steps. The collector is assembled by stacking a cover layer, a spiral channel layer, a microfluidic inlet layer, and a skin-facing sweat collection layer. Then, the assembled collector is mated on an iontophoretically stimulated human forearm's skin for sweat collection. Sequential optical images are taken every 10 minutes.

2.4 Wireless PCB module

The wireless PCB module implements the required excitation circuitries to drive the actuation interfaces (ACET actuation and valving), as well as signal conditioning and processing circuitries to reliably measure the transduced signals (a representative PCB is shown in Supplementary Fig. 2.8). The electrical connections between the microfluidic module and the board can be established

with the aid of a flat flexible cable and an electrically vertically conductive tape (Fig. 2.5b). At its core, the PCB utilized a microcontroller unit (ATmega328 – TQFP, Atmel) that was programmed to facilitate system level functionalities, including setting the operation modes, providing oscillatory control signal to drive the ACET excitation circuitries, and communicating data. These system-level operations can be multiplexed with the use of a bank of digital switches (based on ADG5421 chips, Fig. 2.9). The microcontroller is interfaced with an onboard Bluetooth transceiver to wirelessly and bilaterally communicate the command and sensor output data with a custom-developed smartphone application. The smartphone application provides a graphical user interface for wirelessly activating/deactivating the desired operations (ACET actuation, valving, or sensing) and displaying the sensor output data in real-time.

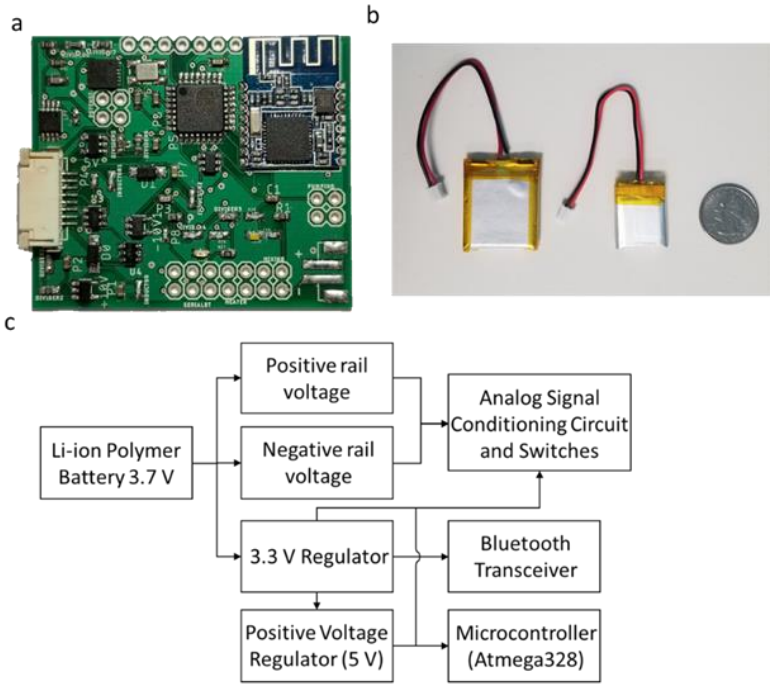

Figure 2.8: Overview of the developed wireless PCB. (a) A representative assembled PCB. (b) Representative rechargeable 3.7 V Lithium-ion battery modules with 150 mAh and 500 mAh capacities (for comparison placed next to a Quarter-dollar coin). (c) Power delivery diagram.

To realize the AC voltage excitation signals driving the ACET actuation electrodes, additional circuitry was needed to overcome the limitations of the microcontroller in generating symmetric sinusoidal signals within the required voltage and frequency range of operations. Accordingly, a push-pull circuit configuration was implemented (Fig. 2.9), which took the microcontroller's Pulse-Width-Modulation (PWM) output as its input control signal, and output a symmetric sinusoidal at 8 MHz (Fig. 2.10a). For valving operation, a digital switch was used to set the voltage across the terminals of the heater electrode, thus controlling the electrical current flow through the heater (Fig. 2.10b).

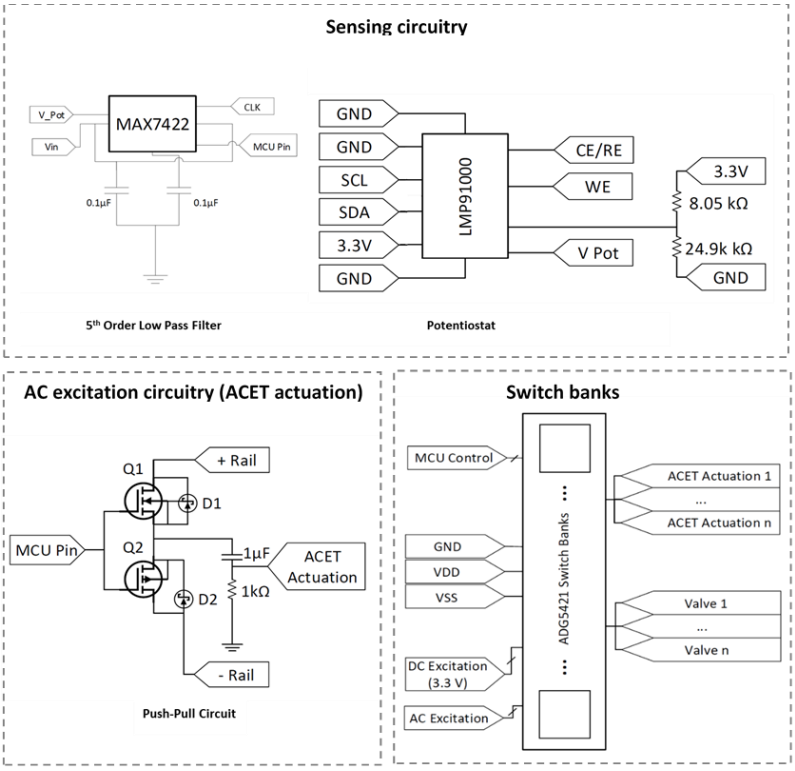

Figure 2.9: Schematic diagrams of the sensing, AC excitation circuitries, and the switch banks.

An illustrative analog signal acquisition and conditioning circuitry was developed to interface the developed amperometric sensors and process the transduced signals. Accordingly, an LMP91000 potentiostat chip (Texas Instruments) was used (Fig. 2.9). This chip was programmed to maintain −0.1 V across the working and reference sensing electrodes, and to convert the transduced sensor current to voltage values by leveraging its internal transimpedance amplifier stage. The output of the potentiostat was connected to a fifth-order low-pass filter (LPF), which was realized by a MAX7422 chip (Maxim Integrated), with a cut-off frequency of 1 Hz. The LPF stage mitigates the high frequency interference and the user motion's artefact. The microcontroller's built-in 10-bit Analog-to-Digital (ADC) unit was used to convert the LPF's analog output to the digital domain. The measured amperometric glucose sensor response by PCB was validated against a potentiostat (CH Instruments, Fig. 2.10c).

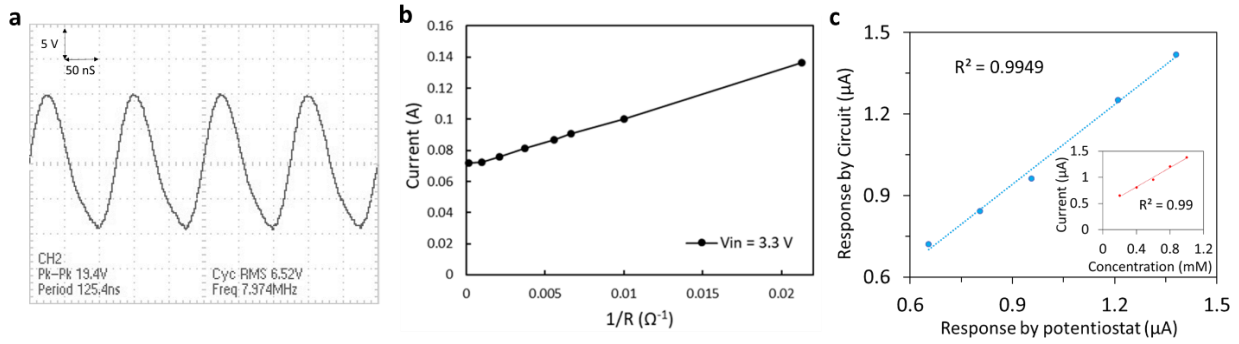

Figure 2.10: Characterization of the output of the excitation and sensing circuitries. (a) A representative push-pull circuit voltage output for ACET actuation. (b) Heater circuit current output level for different resistive loads (with resistance R, applied voltage 3.3 V). (c) The measured amperometric glucose sensor response by PCB *vs.* potentiostat (inset shows the corresponding calibration curve obtained by the potentiostat).

In our PCB development efforts, we selected integrated circuit chips that were designed for low-power applications to implement a power efficient system. To power the PCB, a single miniaturized rechargeable lithium-ion polymer battery with a nominal voltage of 3.7 V can be used. The choice for the battery's capacity depends on the intended modes, duration, and frequency of operations (Fig. 2.9 shows representative 150 and 500 mAh batteries). Based on our characterization results, with no further power optimization, the envisioned simultaneous operations (e.g., ACET actuation, sensing, and bilateral wireless communication) demand supply current levels on the order of 50-100 mA. For an envisioned application such as periodic sweat sampling and analysis at 6 points during the day (e.g., monitoring the glucose levels before/after main meals), and assuming 15 minutes of active operation, a battery capacity on the order of 150 mAh (=6×100 mA×0.25 h) would be needed, while ensuring that the standard discharge requirements are met.

To wirelessly communicate with the PCB module from the user standpoint, an illustrative Android-based smartphone application was developed. The application provides a graphical user interface to execute a range of functionalities, including setting the desired operational modes as well as data display and storage. In our implementation, the user input is read with the aid of touchscreen-activated buttons and relayed to the PCB through communication of pre-defined integer values (each value mapped to a desired operation) using Bluetooth. Then, the corresponding received command is converted to ASCII decimal values for interpretation and execution at the microcontroller level. The representative custom developed application interface and the flow chart of communication commands and corresponding execution steps are shown in Fig. 2.11.

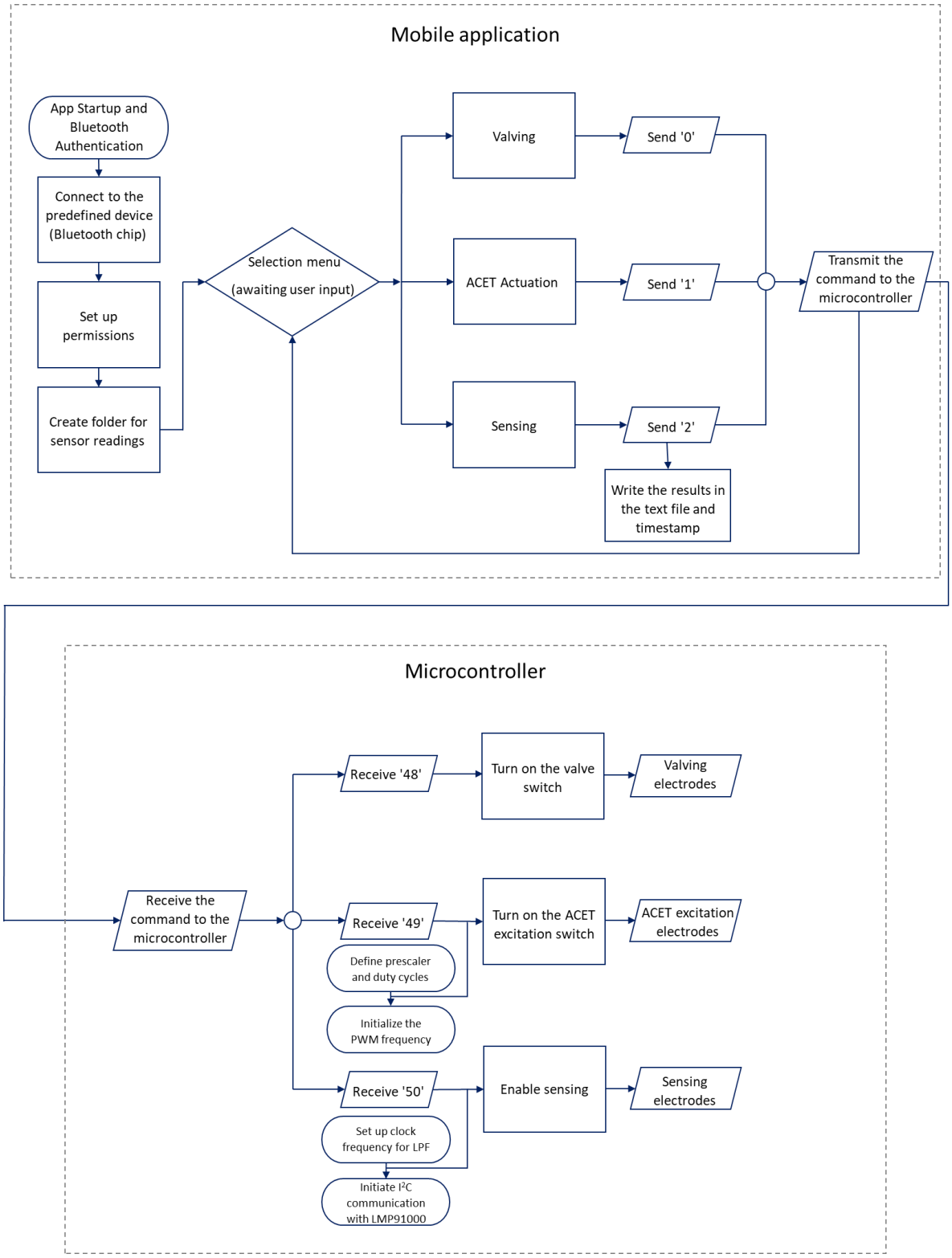

Figure 2.11: Flow chart of the communication commands and execution steps at mobile application-level and microcontroller-level.

Chapter 3 Wearable and programmable ACET actuation

3.1 ACET simulation

ACET-based techniques are suitable for manipulation of biofluids, which have high conductivity [33-38]. ACET originates when a temperature gradient profile ∇T is established in the fluid with the aid of a non-uniform electric field vector E (with magnitude represented as E). This temperature gradient correspondingly produces gradients in permittivity ($\nabla\varepsilon = (\partial\varepsilon/\partial T)\nabla T$) and conductivity ($\nabla\sigma = (\partial\sigma/\partial T)\nabla T$). The interaction of the electric field with these gradient profiles results in body force f_E acting on fluid, as governed by the equation below [33]:

$$f_E = [\frac{\sigma_0\nabla\varepsilon - \varepsilon_0\nabla\sigma}{\sigma_0 + i\omega\varepsilon_0} \cdot E_0]E_0 - \frac{1}{2}E_0^2\nabla\varepsilon \quad (1)$$

, where subscript 0 describes the physical variable at a spatially constant temperature (*e.g.*, E_0 is the electric field at a spatially constant temperature, $T = T_0$).

Electrothermal simulations were performed by using a finite element software (COMSOL Multiphysics 5.2). A comprehensive study on the simulation of the electrothermal behavior of coplanar electrode pairs was previously presented by Meinhart *et al*. [37]. Given the similarity of the electrode and channel configurations, the same approach was adopted to simulate the ACET phenomena. Briefly, the application of an AC voltage across a coplanar electrode pair establishes a non-uniform electric field and subsequently non-uniform temperature, permittivity and conductivity profiles. Consequently, the interaction of the electric field and the charge density distribution ρ, results in a non-zero body force on the fluid. In such a system, the charge distribution must satisfy both the Gauss's law and charge conservation conditions (equations below):

$$\nabla \times E = 0 \quad (2)$$

$$\nabla \cdot (\varepsilon \mathrm{E}) = \rho \quad (3)$$

$$\nabla \cdot (\sigma \mathrm{E}) = -\frac{\partial \rho}{\partial t} \quad (4)$$

By solving the above equations in frequency domain ($\partial/\partial t = i\omega$, where ω is the angular frequency of the excitation voltage) and by applying small permittivity and conductivity gradient approximations, the space charge density ρ can be expressed in a simplified form of [38]:

$$\rho = \nabla\varepsilon \cdot \mathrm{E}_0 - \varepsilon_0 \frac{\mathrm{E}_0 \cdot \nabla(\sigma + i\omega\varepsilon)}{\sigma_0 + i\omega\varepsilon_0} \quad (5)$$

, where the subscript 0 represents the variables for a spatially constant temperature T_0.

In the case of electrothermal kinetics, the temperature gradient-induced permittivity and conductivity gradients can be expressed as

$$\nabla\varepsilon = \varepsilon_0 \alpha \nabla T,\ \nabla\sigma = \sigma_0 \beta \nabla T, \text{where } \alpha = \frac{1}{\varepsilon}\frac{\partial \varepsilon}{\partial T},\ \beta = \frac{1}{\sigma}\frac{\partial \sigma}{\partial T} \quad (6)$$

, where for aqueous solutions at 25 °C, $\alpha \approx -0.0046$ K^{-1} and $\beta \approx 0.020$ K^{-1} [39]. After calculating the space charge density, the electrical body force density can be determined, which is the sum of a Coulomb term and a dielectric term.

$$\mathrm{f_E} = \rho \mathrm{E} - \frac{1}{2} E^2 \nabla\varepsilon \quad (7)$$

Combining (5), (6) and (7), the ACET body force can be expressed as

$$\mathrm{f_E} = [\frac{\varepsilon_0 \sigma_0 (\alpha - \beta)}{\sigma_0 + i\omega\varepsilon_0} \nabla T \cdot \mathrm{E}_0]\mathrm{E}_0 - \frac{1}{2} E_0^2 \nabla\varepsilon \quad (8)$$

In the case of ACET sweat actuation, conductivity and relative permittivity of sweat are 0.6 S/m and 80 respectively and AC frequency is set as 10 MHz. With $\omega \ll \sigma_0/\varepsilon_0$, low frequency approximation can be applied and (8) can be simplified to

$$\mathrm{f_E} \approx -0.022\varepsilon_0 E_0^2 \nabla T \quad (9)$$

which is defined as the body force term in Navier-Stokes equation when simulating laminar flow in the channel.

In the COMSOL Multiphysics simulation setup, laminar flow, heat transfer and electric current physics were employed in the context of a 3D microfluidic channel (with a PET substrate and ceiling), containing a solution with properties similar to that of biofluids (*e.g.*, sweat). The same electrode dimensions were used as the ones used for each experimental setup. Periodic boundary condition was assumed to extend the operation of a single electrode pair to an array of electrode pairs. No-slip boundary condition for the fluid flow was set at the physical boundaries of the channel. The ceiling of the microfluidic channel was set as ambient temperature (25 ^{o}C) and the bottom surface of PET substrate (assumed to be in direct contact with skin) was set as skin temperature. Other surfaces (walls of the channel) were assumed to be thermally insulated. To evaluate the effect of skin surface temperature variation, the ACET simulation was extended to assume a range of temperature values for the skin (10-40 ^{o}C). As an example, this simulation setup was applied to the asymmetric parallel electrode pair configuration (pumping). Figure 3.1 shows the simulated average/normalized flow velocities. These values are obtained by averaging the simulated induced horizontal velocities over the cross-section of the microfluidic channel (100 µm away from the outer edge of the wider ACET electrode), and normalizing with respect to the corresponding case with the skin temperature of 25 ^{o}C. The simulation results indicate that variations in skin temperature have minimal impact on the induced flow, as expected (since the actuation relies on temperature gradient instead of absolute temperature). To characterize the induced ACET-flow velocity *vs.* applied voltage levels and to demonstrate the programmable ACET actuation capability, a function generator (Tektronix, AFG3102C) was used. Accordingly, different voltage values were applied across the ACET electrodes, and optical imaging was performed followed by image analysis to quantify the ACET-induced flow.

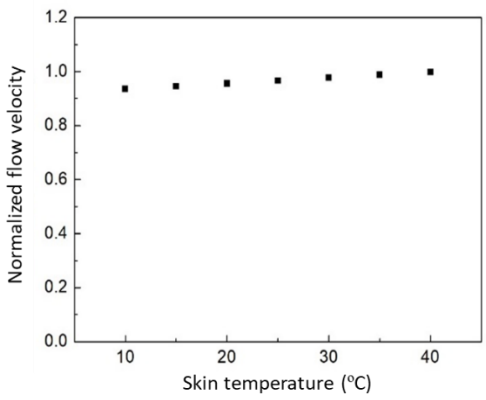

Figure 3.1: Simulated flow velocities with different skin temperature as the boundary condition. The velocity values are obtained by taking the average of the horizontal velocities, over the cross-section of the microfluidic channel, and normalizing with respect to the corresponding case with the skin temperature of 25 °C.

As described by the equation 9, this body force leads to fluid motion with velocity that is proportional to $E_0^2 \nabla T$. For the case where ∇T is induced by the electric field (where $\nabla T \propto E^2$), the velocity becomes proportional to E^4, or equivalently to the 4th power of the applied voltage. Here, the non-uniform electric field is established using coplanar electrodes that are patterned on the bottom of the microfluidic channel (Figure 3.2). The electrodes are excited with an AC voltage source at sufficiently high frequency (8 MHz) to avoid electrolysis and to bypass the double layer capacitance formed at the electrode-buffer interface [26].

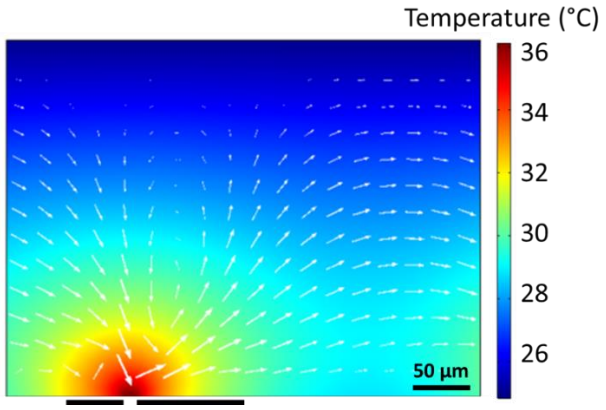

Figure 3.2: Cross-section view of the simulated ACET-induced velocity and thermal profiles of an asymmetric parallel electrode pair (applied voltage: 3.5 V_{RMS}).

3.2 ACET pumping

To realize pumping, asymmetric electrode configurations can be exploited to create directional electro-fluidic flow [33,34]. The asymmetry of the electrode configuration allows for creating imbalanced temperature and electric field profiles, thus breaking the symmetric competitive vortices and consequently inducing directional flow profiles. Here, two configurations of asymmetric electrodes are devised. The first design is based on an asymmetric parallel electrode pair (patterned on the bottom of the channel) consisting of a narrow electrode (width: 40 µm) and a wide electrode (width: 90 µm), separated by 10 µm (Fig. 3.3). As previously postulated for a similar electrode configuration [33], the wide electrode has a larger effective area in terms of fluid induction as compared to the narrow electrode, thus setting the direction of the flow.

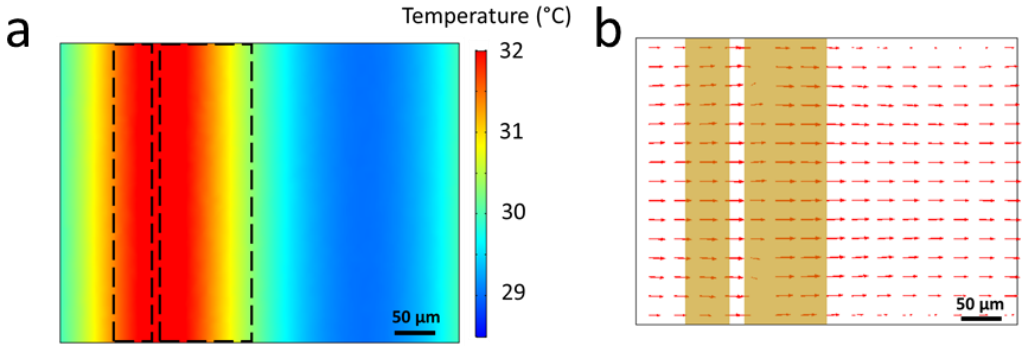

Figure 3.3: (a) Simulated thermal profiles of a pair of parallel asymmetric coplanar electrodes for ACET pumping (50 µm above the ACET electrodes, applied voltage: 3.5 V_{RMS}, narrow electrode width: 40 µm, wide electrode width: 90 µm, electrode spacing: 10 µm). (b) The respective simulated ACET-induced velocity profile for pumping, illustrating a net direction.

As shown in Fig. 3.4, the second design is based on three identical parallel electrodes (width and spacing: 250 µm), which are positioned at a distance of 250 µm with respect to an orthogonally oriented single electrode (width: 250 µm). As speculated in the context of a similar asymmetric electrode configuration [33], the maximal ∇T magnitude spatially occurs in the region between the parallel electrodes' tips and an orthogonally oriented single electrode. As a result, the induced flow in the middle region becomes dominant as compared to that of the surrounding region, resulting in a directional flow.

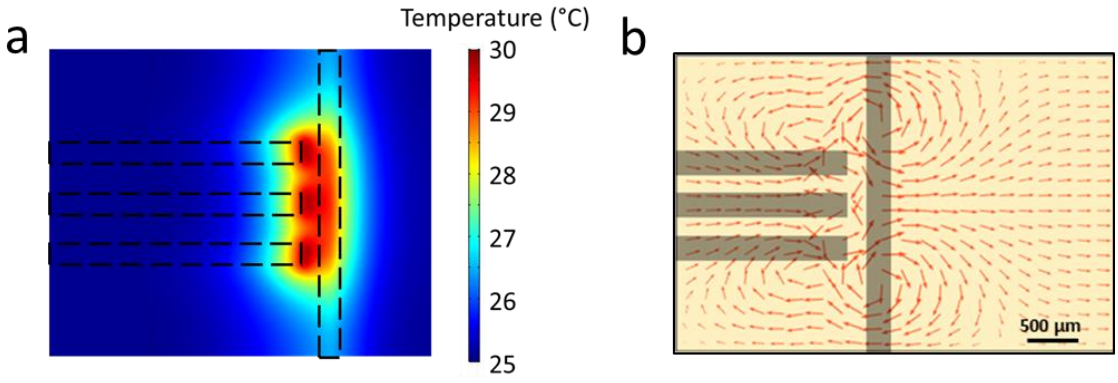

Figure 3.4: (a) Simulated thermal profiles of orthogonal electrodes configuration for ACET pumping. (b) The respective simulated ACET-induced velocity profile for pumping, illustrating a net direction.

The electrothermal simulation results, shown in Fig. 3.3 and Fig. 3.4, verify that the devised asymmetric electrode configurations result in directional flow profiles. To validate and characterize the induced flow by these configurations, 6 μm-diameter beads (Polybead) are introduced in the channel containing the pumping electrodes. By applying different voltage levels, a range of pumping conditions are achieved. The corresponding pumping velocity values are estimated by sequential imaging of the advective motion of the beads (Fig. 3.5a, b). Figure 3.5c, f demonstrate that the measured velocity values, for both configurations, are proportional to the 4^{th} power of the applied voltage, which are in agreement with the velocity-voltage relationship predicted by the electrothermal theory [33].

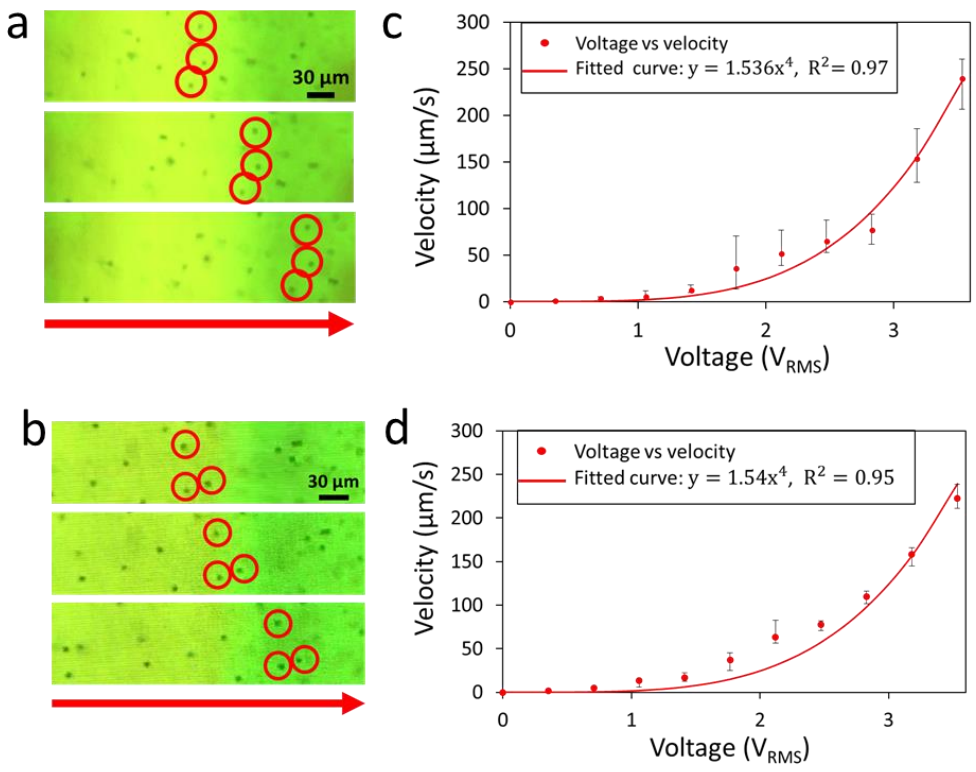

Figure 3.5: Sequential imaging of the advection of microbeads downstream of the channel, due to the generated ACET pumping flow for (a) parallel electrode configuration and (b) orthogonal electrode configuration. Characterization of the induced velocities for a range of applied voltage values for (c) parallel electrode configuration and (d) orthogonal electrode configuration, indicating a 4th power relationship between velocity and voltage.

3.3 ACET mixing

The ACET actuation can be adapted to induce other flow profiles. For example, a rotationally symmetric electrode pair configuration can be used to realize local in-plane micro-vortex flow profile for mixing. As shown in Fig. 3.6, the electrothermal simulation results validate the induction of fluid flow with intended stirring profile.

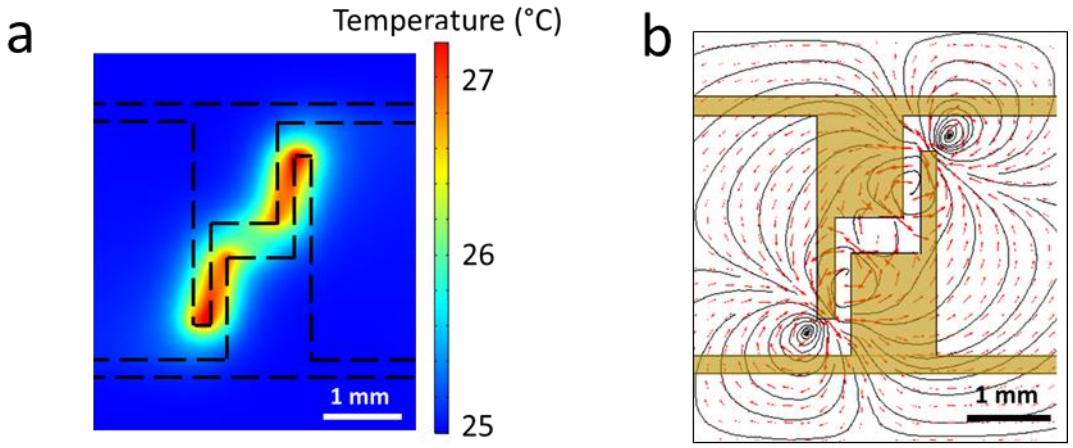

Figure 3.6: (a) Simulated thermal profile of rotationally symmetric electrodes for ACET mixing (50 µm above the ACET electrodes, applied voltage: 3.5 V_{RMS}). (b) The respective simulated ACET-induced velocity profile for mixing, illustrating a vortex-like fluid motion.

In order to evaluate the mixing performance of this configuration, an array of this electrode pair is used to induce mixing of two neighboring injected laminar fluid flows (one blank artificial sweat, another dyed artificial sweat, injected by two syringe pumps in parallel) downstream of a reverse bifurcated channel (Fig. 3.7). In this way, the effect of locally generated flow vortices (as induced by these electrodes) can be characterized against advection-driven flow profiles.

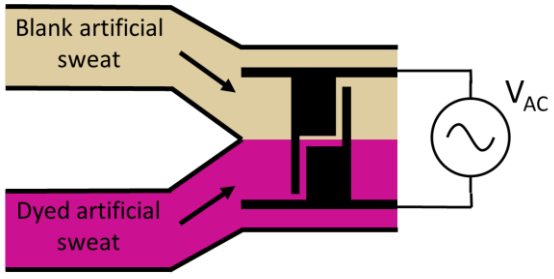

Figure 3.7: Experimental setup to characterize the ACET-induced vortex flow against externally driven advection flow for evaluation of the mixing efficiency.

To quantify the ACET-induced mixing efficiency, similar to previous efforts [31]the mixing of two side-by-side laminar flows (one containing blank artificial sweat, the other containing red-dyed artificial sweat) was characterized for various excitation voltages and flow velocities. Accordingly, the microfluidic region containing the mixing electrode array was video-recorded. The corresponding video frames were subsequently imported into MATLAB (Mathworks). The boundaries of a pair of electrodes were identified at the software level, and the image analysis was performed in its neighboring region. Similar to previous work [31], a mixing index is defined, as expressed below, that calculates the reciprocal of the standard deviation s of the local dye density in the imaged region:

$$\text{Mixing index} = \frac{1}{s} = \sqrt{N / \sum_{i=1}^{N} (c_i - c_{\text{ave}})^2} \quad (10)$$

where N, c_i, and c_{ave} are the total number of pixels in the neighboring region, the intensity at pixel i, and the average intensity over N pixels, respectively. With this definition, the higher the index value, the lower the standard deviation, and the more homogenized the local dye density in the imaged region. To normalize our readings, this index is linearly mapped over the range of 0 to 1, where 0 corresponds to the initial state (negligible mixing), and 1 corresponds to the fully-mixed steady state.

In this way, the mixing index effectively captures the reciprocal of the standard deviation of the local dye density in the imaged region (the higher the index value, the lower the standard deviation, and the more uniform the local dye density in the imaged region). This index is linearly mapped over the range of 0 to 1, where 0 corresponds to the initial state (negligible mixing), and 1 corresponds to the fully-mixed steady state (Fig. 3.8 inset). Due to its electro-fluidic nature, this

mixing capability can be precisely tuned by programming the applied voltage at the electrodes (Fig. 3.8).

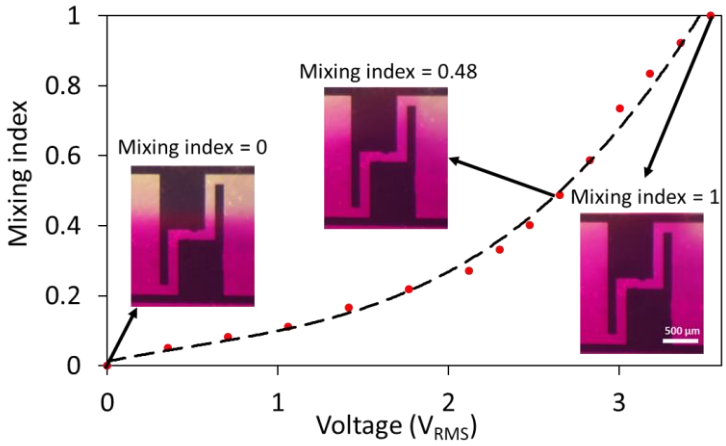

Figure 3.8: Mixing efficiency for a range of applied voltage values (externally driven advection flow: 5 µL/min). Inset includes the optical images corresponding to mixing indices of 0, 0.48 and 1.

The robustness of the induced stirring motion is evaluated by characterizing the mixing index for a range of flow rates. Figure 3.9a demonstrates that near full mixing is achieved (applied voltage of 3.5 V_{RMS}) for the flow rates as high as 100 µL/min. Additionally, as shown in Fig 3.10, our stability characterization results indicate robust ACET actuation for extended amount of time (> 8 hr) and at high ambient temperature values (*e.g.*, 40 °C). The wearable ACET actuation method is validated through performing on-body experiments with the microfluidic module worn on the volar surface of the forearm, as illustrated in Fig. 3.9b.

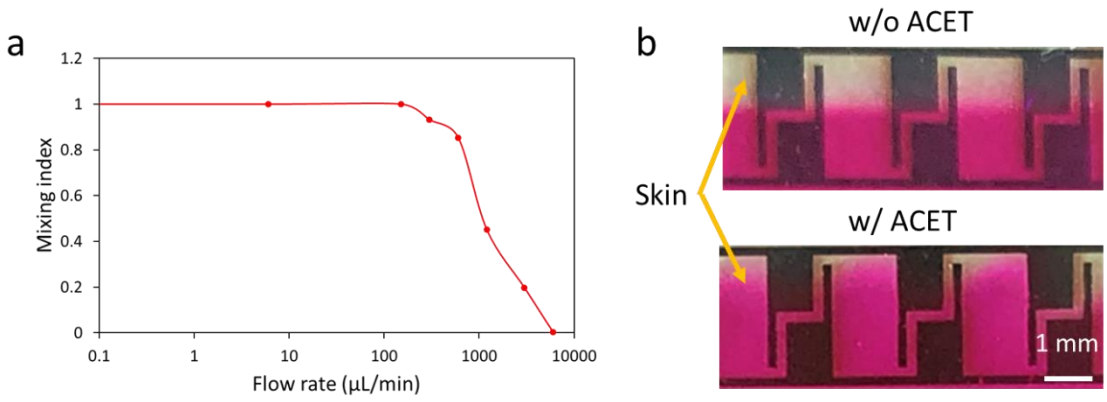

Figure 3.9: (a) Characterization of mixing efficiency for a range of advection flow rates, indicating that near full mixing is achieved for flow rates as high as 100 µL/min (applied voltage: 3.5 V_{RMS}). (b) Visualization of ACET mixing on body.

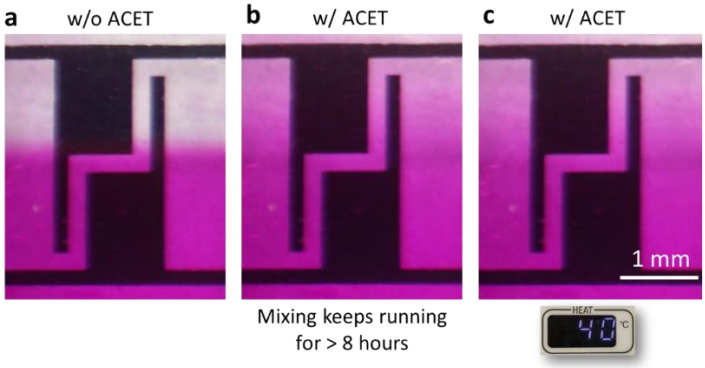

Figure 3.10: Optical imaging of the ACET electrodes, when ACET actuation is (a) deactivated. (b) activated, > 8 hr of operation at the room temperature. (c) activated, with surrounding temperature of 40 ^{o}C.

Chapter 4 Wearable valving: model, design, and characterization

4.1 Thermoresponsive hydrogel for valving

Here, a binary off/on valve operation is desired, where fluid flow is completely blocked with no leakage in "off"-state (valve closed), and fluid flow is permitted in "on"-state (valve open). The operation of the wearable microfluidic valve is based on the shrinkage and expansion of a thermal-stimuli-responsive hydrogel [40-44] (embedded in the microfluidic channel, Fig. 4.1 upon activating and deactivating a programmable microheater that is patterned on the bottom of the channel).

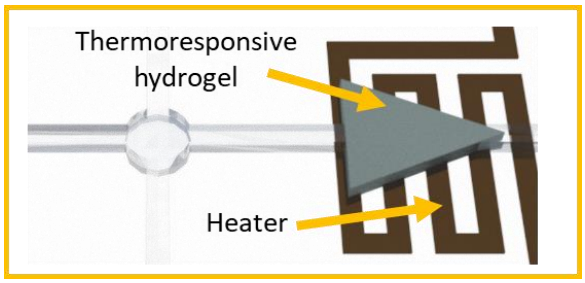

Figure 4.1: Schematic of PNIPAM-based hydrogel valve in microfluidic channel.

We specifically use a modified poly(N-isopropylacrylamide) (PNIPAM)-based hydrogel. This hydrogel significantly shrinks/expands in response to local temperature increments/decrements, around its lower critical solution temperature (LCST), and correspondingly, permits/blocks fluid flow. The thermal responsive hydrogel was prepared by mixing 0.545 g NIPAM (Sigma-Aldrich), 0.030 g N,N′-methylenebisacryl-amide (Sigma-Aldrich), 0.75 mL dimethyl sulphoxide (Sigma-Aldrich), 0.25 mL deionized water, 0.010 mL [3-(methacryloylamino)propyl]trimethylammonium chloride (MAPTAC, Sigma-Aldrich) solution (50 wt. % in water), and 0.0385 g 2,2-dimethoxy-2-phenylacetophenone (DMPA, Sigma-Aldrich). This mixture was then sonicated in a water bath for 15 min at 48 ^{o}C with sonication frequency of 40 kHz. Next, the mixture was cast in a mold with

the desired shape (e.g., circle for characterization and triangle for operation), and photo-polymerized with the aid of UV photolithography (UV intensity of 8 mW/cm^2 and exposure time of 18 s). The prepared hydrogel was then inserted into form-fitting microfluidic channels (Fig. 4.2). To characterize the hydrogel shrinkage with respect to controlled temperature increments, a hot plate (Fisher Scientific) was used. A DC power supply (Keithley 2230-30-1 Three-Channel Programmable DC Power Supply, Keithley Instruments Inc.) was used to drive the microheater (patterned at the bottom of the hydrogel-embedded microfluidic channel), in order to characterize the hydrogel's periodic reversible response. Optical imaging was performed followed by image analysis to quantify the changes to the hydrogel size.

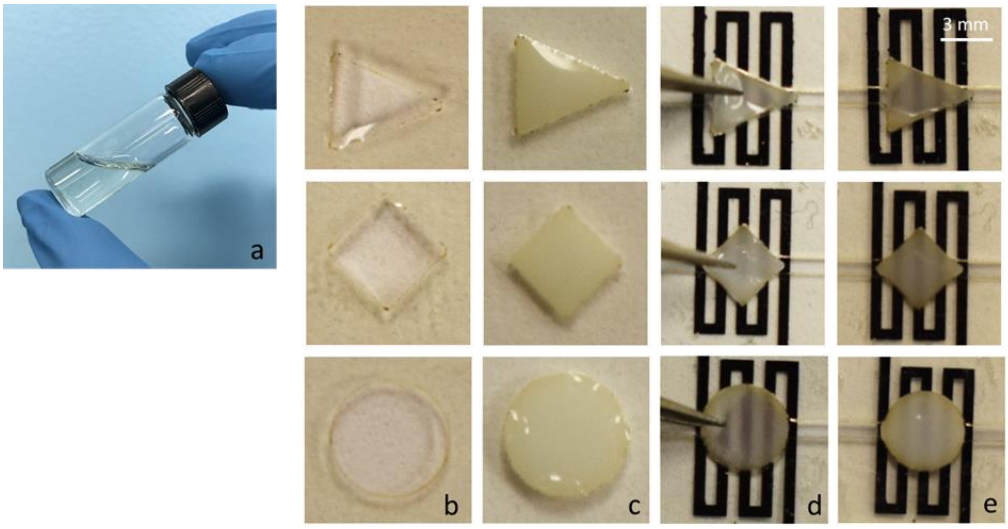

Figure 4.2: Hydrogel synthesis and assembly procedure (with different representative shapes). a) Chemicals (as described in the Method section) are mixed in the liquid phase. b) Liquid phase solution is injected into mold. c) Image of hydrogel after cross-linking by UV. d) Hydrogel is embedded into the microfluidic channel. e) PET cover of the microfluid channel is placed on top.

For robust on-body valving, the LCST should be sufficiently above the skin temperature of ~35 °C, such that the heat transfer from the skin to the valve does not result in significant hydrogel

shrinkage and subsequent fluid leakage. Conventional PNIPAM-based hydrogels with LCST values of about 32 °C [42] would not meet this constraint. Therefore, the LCST of the PNIPAM-based hydrogel is adjusted to ~45 °C by incorporating an ionizable monomer (MAPTAC) in the hydrogel structure [43]. The inherent design of the multi-layer microfluidic module prevents the direct contact of the heater substrate with the skin and mitigates conspicuous increase in skin temperature.

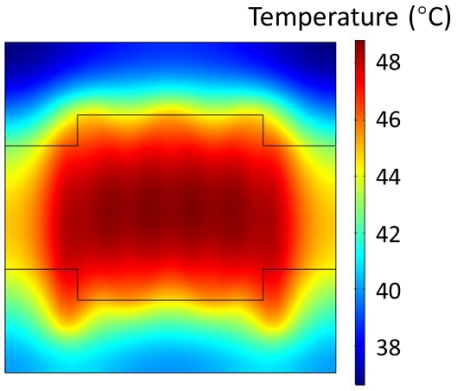

Figure 4.3: Simulated thermal profile of the heater, illustrating joule heating in a microfluidic channel.

4.2 Simulation of microheater

The microheater is constructed as a serpentine-shaped electrode (total length: 32 mm, width: 0.5 mm, thickness: 130 nm, resistance ~40 Ω). The thermal simulation results shown in Fig. 4.3 demonstrate that upon applying voltage across the electrode, the resultant resistive joule heating increases the local temperature. As shown in Fig. 4.3, to simulate the electrothermal behavior of the heater component of the valve, heat transfer and electric current physics were employed in a similar 3D model described above (microfluidic channel with PET substrate, ceiling and wall and biofluids inside the channels). The electrode dimensions were the same as the one used in the

experiments. The ceiling of the microfluidic channel and the bottom surface of PET substrate were set as ambient temperature (25 ^{o}C) and the other surfaces (walls of the channel) were assumed to be thermally insulated. The temperature profile in the microfluidic channel was simulated by coupling heat transfer and electric current (joule heating).

4.3 Characterization of thermoresponsive hydrogel

As shown in Fig. 4.4, the embedded PNIPAM-based hydrogel exhibits about 25% shrinkage from its original size (based on the 2D imaged area) when ramping up the temperature above its LCST point. Reversibly, the hydrogel can recover to its original volume, simply by de-activating the heater.

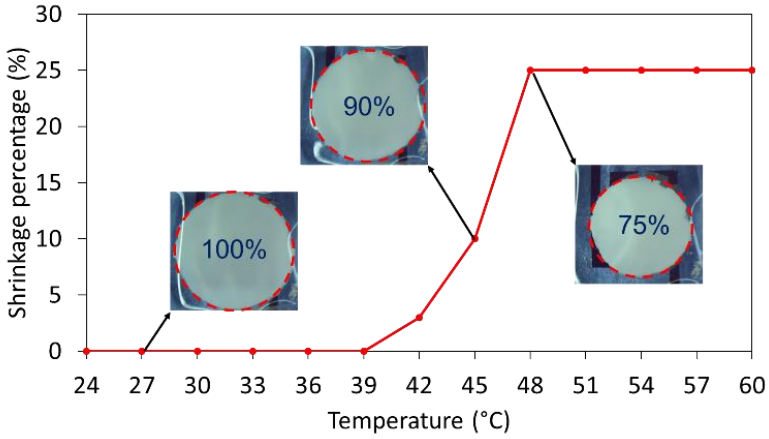

Figure 4.4: Hydrogel shrinkage vs. temperature profile. The microscopic images of the hydrogel at three different temperatures are shown as inset.

Figure 4.5 illustrates that the periodic activation and deactivation of the heater result in reversible shrinkage and expansion of the hydrogel with consistent switching profile. The observed asymmetry in the rise time *vs.* fall time of the respective hydrogel shrinkage profile can be

attributed to the difference in the outward and inward diffusion rate of the surrounding buffer solution into the hydrogel [41].

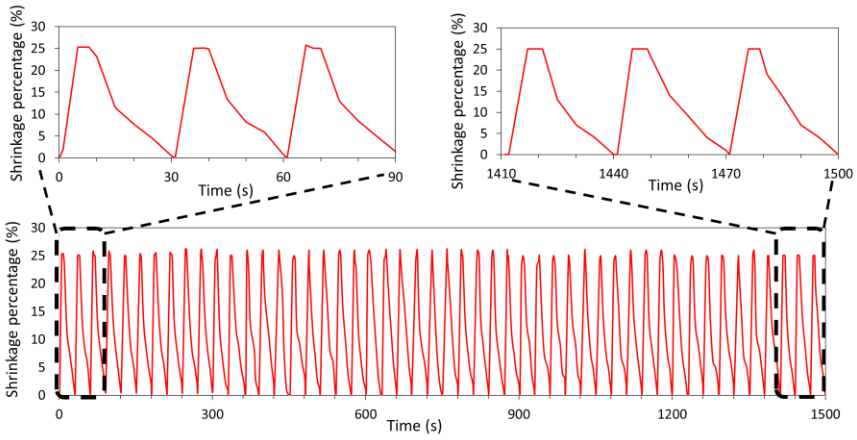

Figure 4.5: Periodic and reversible valving with consistent switching profile (50 cycles).

4.4 Valving characterization for on-body operation

The intended valve operation is validated through performing on-body experiments with serial and parallel valving configurations. For serial valving, along with a single microfluidic channel, two valves are incorporated in series. Figure 4.6 demonstrates the controlled blockage and permission of the flow of the introduced red-dyed artificial sweat, through a sequential opening of the two valves on-body. The parallel valving configuration is comprised of a T-shaped microfluidic channel and two valves. The valves can be selectively opened and closed to permit and block the fluid flow through their respective downstream channels.

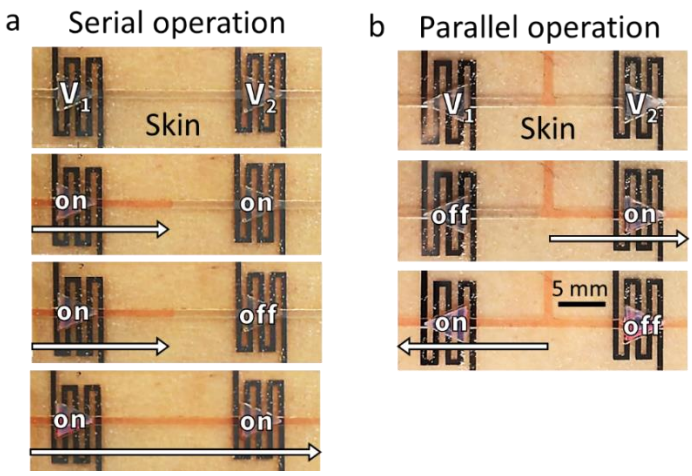

Figure 4.6: Validation of microfluidic valving on body to perform serial (a) and parallel operations (b). The sequences of images show the consecutive/selective blockage and permission of the flow through controlling the valves. The white arrow tracks the liquid flow.

The robust valving performance can be maintained for longer than 8 hours and at the high ambient temperature of 40 °C (Fig. 4.7). Successfully valving operation (as it can be seen from the blue liquid pass the valve) is demonstrated by turning the heater on.

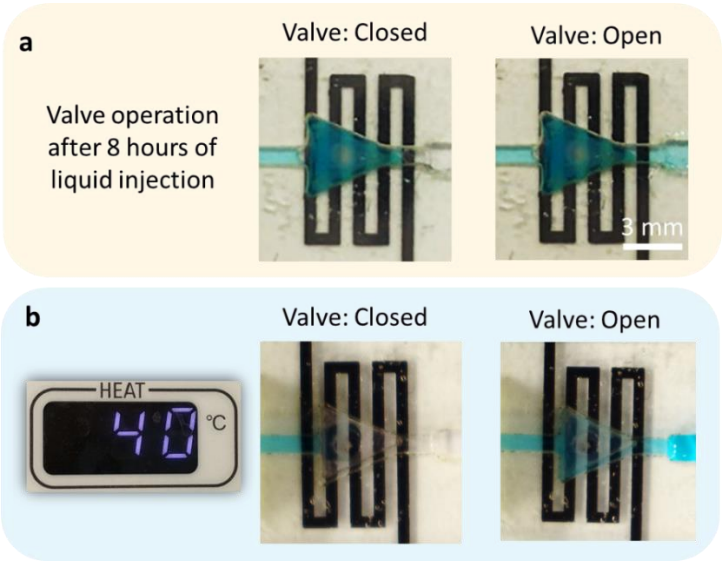

Figure 4.7: Stability of valving operation. Optical imaging of valve, with a blue-dyed liquid in the microfluidic channel a) Valving operation after > 8 hr of the injection of the blue-dyed liquid (at the room temperature). b) Valving operation with the surrounding temperature of 40 ^{o}C.

4.5 Valving interface with sweat glands: an electronic-hydraulic analogy

In order to adapt the demonstrated valving capability for sampling, routing, and compartmentalizing sweat, directly harvested from glands, pressure release mechanisms need to be devised to avoid pressure built-up across the glands or the valve breakage caused by the high pressure secreted sweat (with pressure as high as ~500 mmHg with air-tight sealed interface [45]). As shown in Fig. 4.8, the problem at hand can be analogically likened to a circuit configuration consisting of a current source that enforces the delivery of a current level I_s through a series combination of an electrical resistor (with resistance R_e) and a temperature-controlled transistor (acting as a switch, with breakdown potential V_b). The current source, electrical resistance, and the transistor functionality are correspondingly analogous to the sweat gland (secreting sweat rate Q_s), hydraulic resistance of the channel (R_e), and the valve (with breakage pressure P_b). In the same way that the series resistor and transistor, in its off mode, connected to the current source leads to high potential difference (> V_b) across the transistor, causing the transistor breakdown, the air-tight interface of the microfluidic channel and closed valve with the sweat gland results in high pressure difference (> P_b) across the valve, leading to the valve breakage (Fig. 4.8a).

In both scenarios, the addition of a secondary parallel conductive path (with electrical and hydraulic resistance of $R_{e,s}$ and $R_{h,s}$) allows for redirecting the electrical current/fluid flow as a relief mechanism (Fig. 4.8b). In the revised configuration, the potential/pressure difference appearing across the transistor/valve becomes $I_s R_{e,s}$ and $Q_s R_{h,s}$,which with the appropriate design

choice can be set to well-less than V_b and P_b. Accordingly, we devise a T-junction configuration to connect the fluid input port to the valve, where the secondary arm serves as a pressure release channel. To mimic the sweat gland secretion functionality, a syringe pump is connected to the fluid input port, which can be programmed to inject series of increasing flow rates. As shown in Fig. 4.8c , our characterization results indicate that the devised pressure-release configuration can withstand injected fluid flow rates as high as 5000 µL/min.

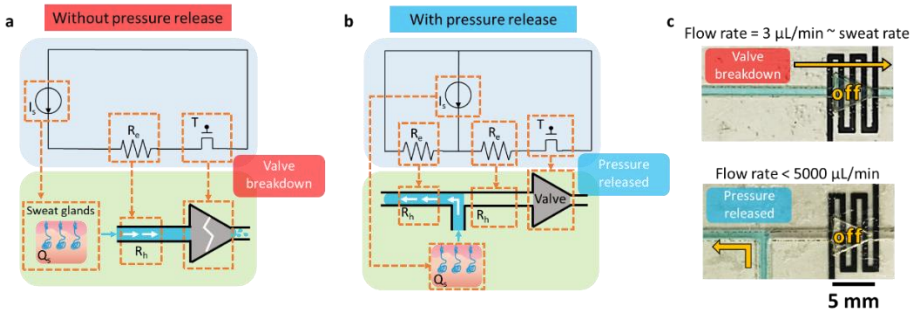

Figure 4.8: a) Analogous electronic-hydraulic configurations and b) the use of secondary electrical current/fluid flow pathways as relief mechanisms. c) The devised pressure-release configuration withstands injected fluid flow rates as high as 5000 µL/min.

Chapter 5 Amperometric sensor development and characterization

5.1 Basis of operation

To demonstrate electrochemical sensing capability and as a proof of concept, here, we develop enzymatic sensor interfaces (patterned within our microfluidic module), which have been shown to be useful for the sensing a wide panel of biomarkers including metabolites (e.g., glucose and lactate) on-body. Accordingly, we specifically, devise H_2O_2-based enzymatic sensing interfaces. This is because H_2O_2 is the byproduct of oxidases (*e.g.*, glucose oxidase) that are often used as biorecognition elements.

5.2 Amperometric sensor development and characterization

To develop the H_2O_2 sensor, a Prussian blue (PB) mediator layer was deposited onto the Au-patterned electrodes (1 mm*1 mm) by cyclic voltammetry from 0 to 0.5 V (*vs.* Ag/AgCl) for one cycle at a scan rate of 20 mV/s in a fresh solution containing 2.5 mM $FeCl_3$, 100 mM KCl, 2.5 mM $K_3Fe(CN)_6$, and 100 mM HCl. Then, a 1% chitosan solution (Sigma-Aldrich) was prepared by dissolving chitosan in a 2% acetic acid (Sigma-Aldrich) and stirring for about 30 min. By drop casting 0.5 μL chitosan solution onto Au/PB electrode, the H_2O_2 sensing interface was realized. To create the glucose sensor, the aforementioned 1% chitosan solution was mixed thoroughly with a glucose oxidase solution (Sigma-Aldrich, 50 mg/mL in PBS, pH 7.2) at a ratio of 1:1 (volume/volume). By drop casting 1 μL of the mixture onto the Au/PB electrode, the glucose sensing interface was realized. To create the choline sensor, a 0.5 μL choline oxidase solution (Sigma-Aldrich, 0.5 unit/μL in DI water, pH 7.2) was placed onto Au/PB electrode and dried at room temperature, followed by drop casting of 0.5 μL 1% chitosan solution (Fig. 5.1). Sensors were allowed to dry overnight at 4 °C, while being protected from light. The sensor was stored at

4 °C when not in use. For all amperometric sensors, the reference/counter electrodes were fabricated by depositing Ag/AgCl ink (Ercon) on electrodes and heating the modified electrodes at 80 ºC for 10 min.

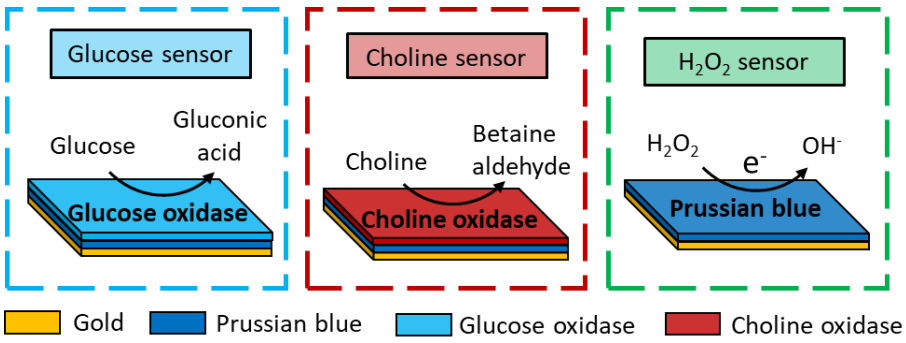

Figure 5.1: Glucose, Choline and H_2O_2 sensing mechanism interface.

To characterize the developed sensing interfaces, constant potential amperometric measurements were conducted in PBS buffer (pH = 7.2) at -0.1 V *vs.* Ag/AgCl. The chronoamperometric response was recorded by a potentiostat (CH Instruments) for 60 s. Calibration plots were obtained by introducing different concentrations of the targets (*e.g.*, H_2O_2, glucose, and choline) in the PBS buffer (Fig. 5.2). Accordingly, the limit of detection (LOD) for each amperometric sensing interface was calculated as $LOD_{glucose}$: 17.6 µM, $LOD_{choline}$: 7.2 µM, and LOD_{H2O2} : 3.9 µM (LOD = 3SD/slope, where SD is the standard deviation of the baseline noise in blank solution).

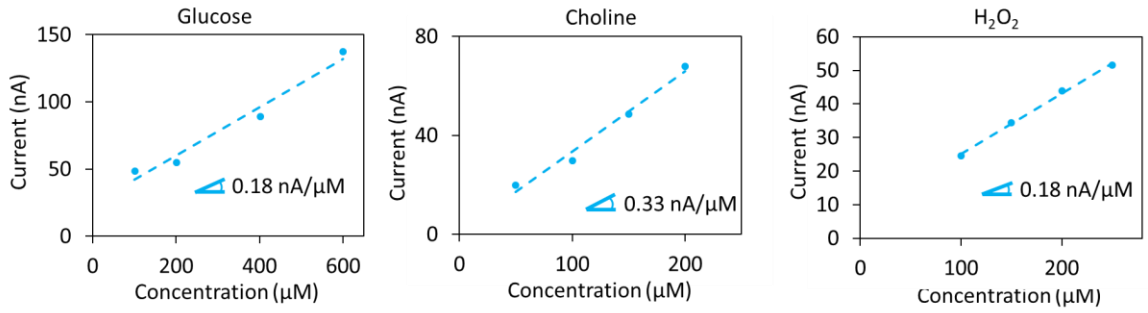

Figure 5.2: Calibration plot of glucose, choline and H_2O_2 sensor.

Chapter 6 System level integration with clinical utility

6.1 Wearable valving for biofluid compartmentalization and temporal sweat sampling

To demonstrate the pressure-balanced valving capability for *in-situ* sweat sampling, routing, and compartmentalizing, a 3D microfluidic architecture is used (Fig. 6.1). This architecture contains three orthogonally-positioned microfluidic valve-controlled compartments and a single pressure-release channel in one layer(Fig. 6.1b). The center of this cross-shaped configuration is connected to a sweat collection chamber underneath in order to interface the skin (Fig. 6.1a). The three-compartment interface can be programmed to direct and compartmentalize sweat samples at various desired time-points (while avoiding mixing with old samples). Here, the pressure-release channel also serves as a waste channel for discarding unwanted sweat samples, for example, the initially secreted contaminated sample [46,47] or the secreted sweat at undesired time-points.

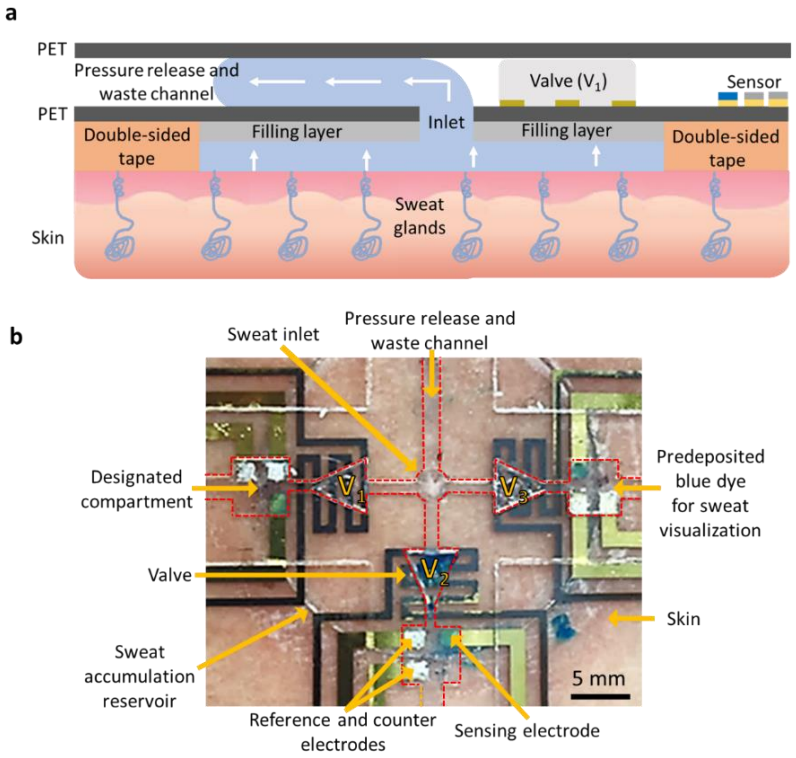

Figure 6.1: A 3D multicompartment microfluidic architecture for in-situ sweat sampling, routing, and compartmentalizing. a) Cross-view (diagram) and b) top-view (annotated photo) of the device interfacing the skin surface.

As shown in Fig. 6.2, initially, when the corresponding valves of all three compartments are closed, the iontophoretically-stimulated sweat is directed through the pressure release/waste channels. Then, to direct the secreted sweat sample into the desired compartment, the corresponding valve of that compartment is opened, while closing the remaining ones, which is illustrated here as a sequential set of operations.

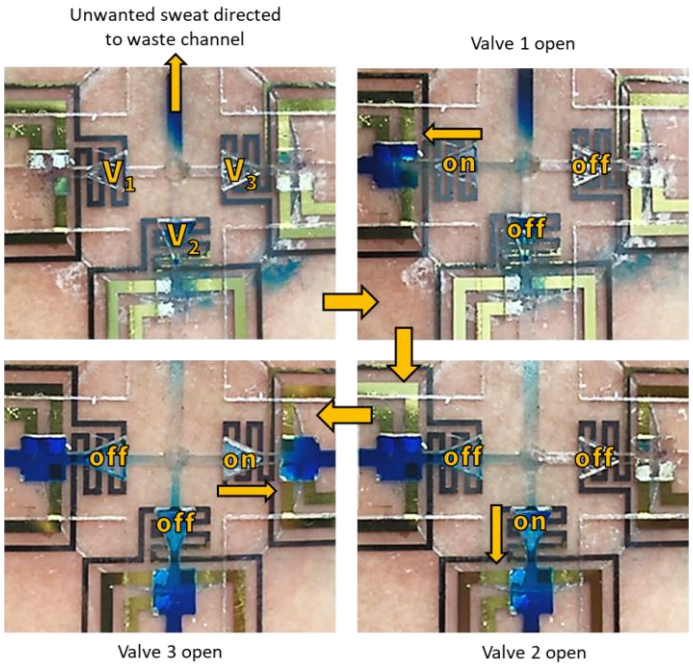

Figure 6.2: Sequential multi-compartmentalization for autonomous temporal sampling (direct epidermal interface is achieved with vertically integrated microfluidic sweat collector underneath).

Biofluid sample compartmentalization is generally useful to prevent mixing of new and old samples and to obtain undistorted estimates of biomarker levels. To illustrate this point, the readout

of an enzymatic glucose sensor, integrated within a single compartment, was sequentially recorded in response to three consecutively introduced spiked samples (Phosphate Buffered Saline, PBS, spiked with different glucose concentrations, sensor development and calibration descriptions are detailed in the Methods section). A similar procedure was performed with a group of three compartments, where each compartment was designated to analyze one sample. The determined glucose concentrations by the single microfluidic compartment ($C_{S,1}$ to $C_{S,3}$) and each of the three microfluidic compartments (C_1 to C_3) are plotted against the expected glucose concentrations, as shown in Fig. 6.3. The results demonstrate that the single microfluidic compartment configuration underestimates the glucose concentration for the subsequently introduced samples (after the first sample), due to sample contamination with previous samples (slope: 0.48). On the other hand, the multi-compartment sensor readouts are in line with the expected glucose concentrations (slope: 1).

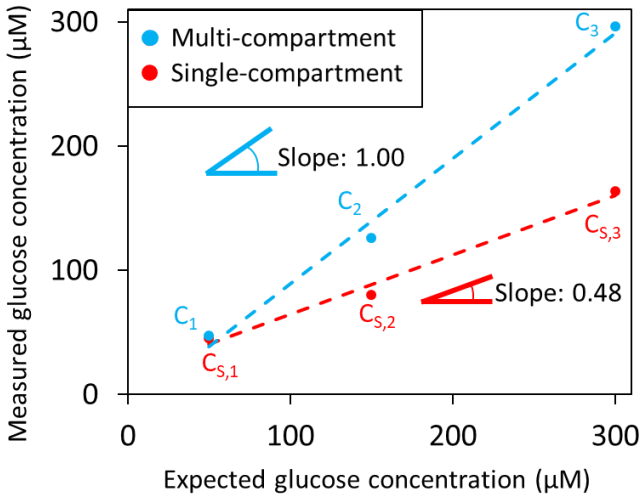

Figure 6.3: Comparison of the determined glucose concentrations of three consecutively introduced spiked samples, as collected by a multi-compartment configuration vs. single-compartment.

Furthermore, the multi-sample compartmentalization capability is particularly useful for the characterization of sweat biomarker temporal profiles (*e.g.*, diurnal profile or excursion profile upon consumption of meal), where autonomous frequent sweat sampling is needed, while preventing mixing with contaminated/old sweat samples [15]. Here, as a proof of concept, we applied the multi-compartmentalized interface to characterize the increasing sweat glucose trend upon glucose intake (50g). Accordingly, standard iontophoresis protocol [48] was used to perform sweat stimulation on the volar surface of a subject's left forearm. Then, the cross-shaped microfluidic configuration was placed on the stimulated area to take three intermittent sweat samples (~5 μL), after glucose solution consumption. For this experiment, the compartments were programmed to take sequential samples of sweat at minutes 15, 27, and 33. These time-points are selected within a time-window that allows for discarding the initially contaminated sweat [46, 47], while maintaining a relatively stable sweat secretion rate [11]. As a 'control' experiment, to validate the autonomous multi-compartment device's capability of fresh sweat collection, the same iontophoresis stimulation step was performed on the subject's right forearm at the same time, followed by a sequence of manual sweat collection (every 3 minutes). Figure 6.4 shows that the sweat glucose concentrations of the analyzed samples for both left and right forearms are similar in value (for the respective selected time-points) and mirror the increasing trend of blood glucose (measured by fingerstick technique).

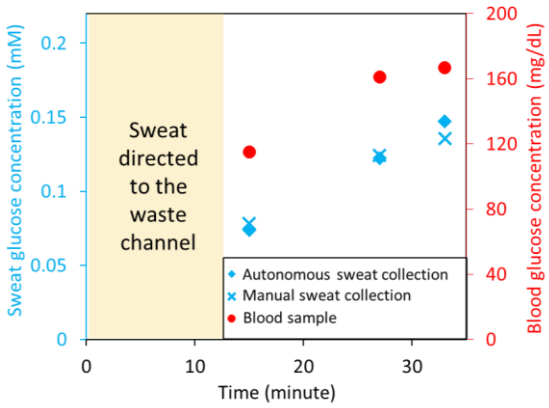

Figure 6.4: Increasing concentration of glucose in iontophoretically-stimulated sweat and blood upon glucose intake. The sweat glucose levels in multi-compartmentalized and manually collected sweat samples are closely correlated and mirror the increasing trend of blood glucose.

As shown in Fig. 6.5, the obtained sweat *vs.* blood glucose trends were further validated (within the same time window) by performing additional human subject trials (3 subjects), following the described 'control' collection procedure. Overall, these results validate the intended operation of our autonomous sweat sampling methodology to collect on-demand, time-stamped, and undistorted sweat samples.

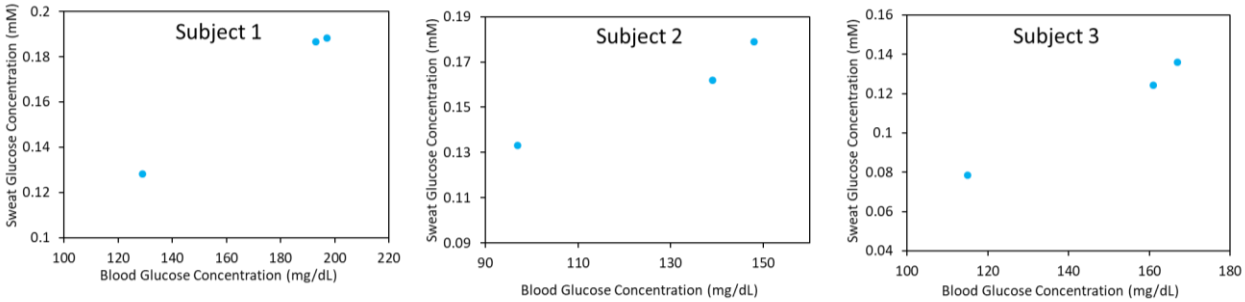

Figure 6.5: Increasing glucose concentration in sweat and blood upon glucose intake, obtained within the same time window as Fig. 3h (3 subjects).

6.2 Multi-on-demand and enhanced sensing system

The demonstrated biofluid actuation-enabled 3D microfluidic architectures, with autonomous functionalities, provide additional degrees of freedom for sensor implementation to enhance the performance of the existing sensing interfaces. For example, by leveraging the devised vertical assembly approach, the prepatterned sensing and actuation interfaces can be aligned and faced toward each other to form a sandwiched-like configuration, capable of simultaneously actuating and sensing biofluid (Fig 6.6).

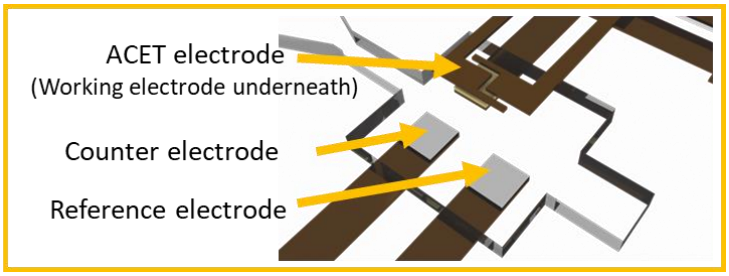

Figure 6.6: Schematic of ACET actuation-enhanced amperometric sensing interface.

Here, we specifically exploit this capability to demonstrate the enhancement of glucose, choline and hydrogen peroxide (H_2O_2) sensor responses (as examples of amperometric electrochemical sensing interfaces) in presence of ACET actuation. Accordingly, as shown in Fig. 6.7, we use a similar cross-shaped multi-compartment design as the previous section, with sensing and ACET actuation electrodes prepatterned onto the substrate and ceiling layers, respectively, and vertically interfaced (within each of the designated compartments).

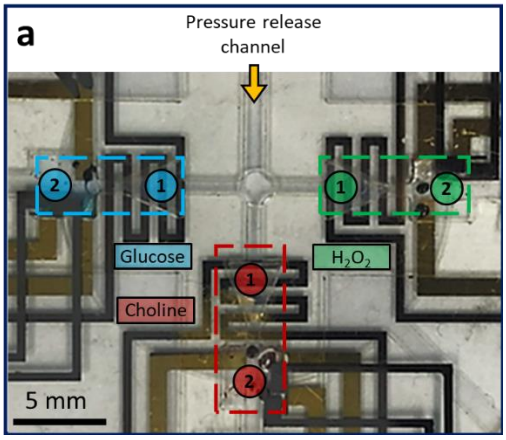

Figure 6.7: A multi-compartment configuration for the analysis of Glucose (blue compartment), Choline (red compartment), and H_2O_2 (green compartment) using ACET actuation-enhanced amperometric sensing surfaces. The entrance of each compartment is controlled by a designated valve (component ①). Within each compartment, the amperometric sensor interfaces a vertically aligned ACET actuator (component ②).

By specifically functionalizing the sensing electrodes of each of the compartments, the multi-compartment configuration can be adapted to perform multi-on-demand sensing–where the sensing of the target analyte(s) can be achieved by independently/simultaneously activating the corresponding compartment(s). In our implementation, shown in Fig. 6.8, the blue-, red-, and green-outlined compartments are correspondingly designated for glucose, choline and H_2O_2 sensing (sensor development description is detailed in the Methods section). The calibration curve of each of the ACET actuation-assisted (3.5 V_{RMS}) amperometric sensing interfaces is obtained and compared to the corresponding calibration curve of the cases where ACET actuation was not activated (also shown in Fig. 6.9).

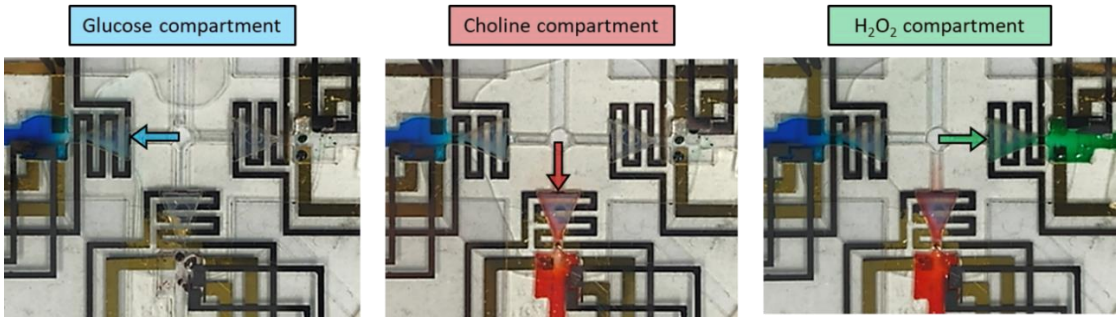

Figure 6.8: Sequential images of different analyte solutions entrance the corresponding compartments. (Color dye is predeposited in the sensing chamber to show the filling of solution)

To characterize the ACET actuation-enhanced sensor response, the sandwiched-like device configuration, containing the actuation/sensing electrodes, was used (as described in the main text). To drive the ACET actuation electrodes, a function generator (Tektronix, AFG3102C) was used. To compare the effect of ACET actuation on the sensor response, first, the calibration plot for the case of no ACET actuation was obtained, as described before. Then, the calibration plot of the sensor in presence of ACET actuation was obtained by applying 3.5 VRMS (10 MHz) across the ACET electrodes and recording of the sensor's chronoamperometric response (after a quiet time of 10 s), while ACET actuation remained activated. To characterize the response time of the amperometric sensor, the response time was defined as the time taken for the absolute gradient of current signal (|di(t)/dt|), normalized with respect to the absolute signal value (|i(t)|), to fall below a given decay rate ε (here, selected as 2% per second), following the expression below [49]:

$$T_{\mathrm{R}} = \min\left\{t: \left|\frac{1}{i(t)} \cdot \frac{\mathrm{d}i(t)}{\mathrm{d}t}\right| < \varepsilon\right\} \quad (11)$$

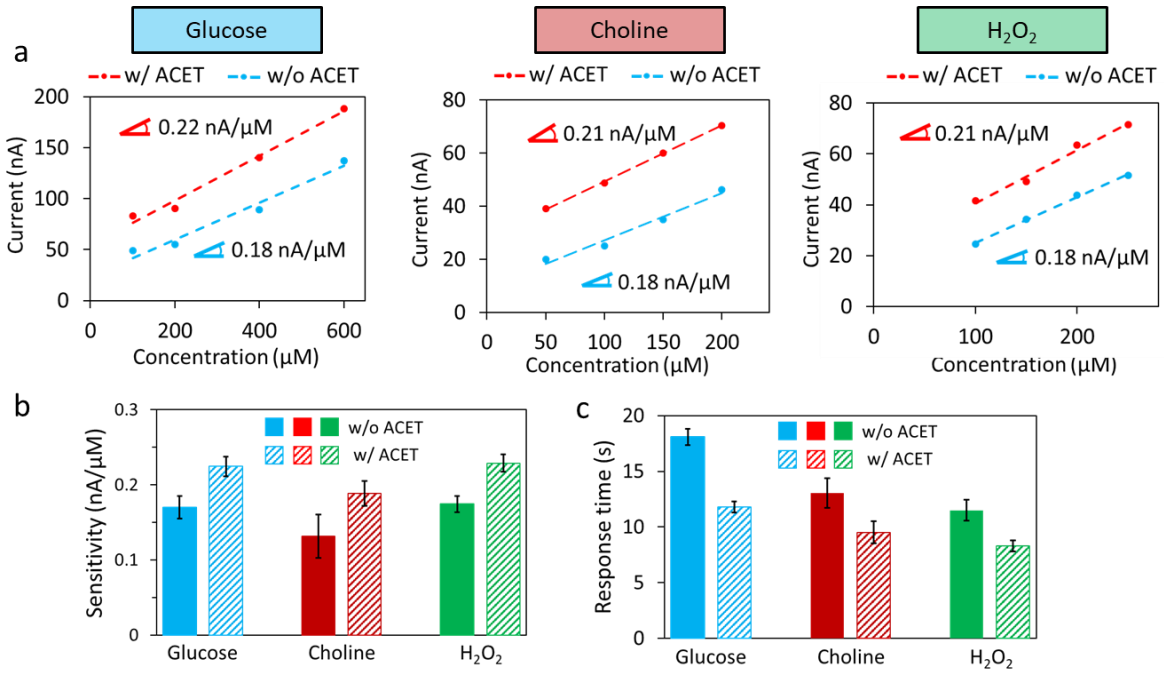

Figure 6.9: a) Comparison of sensing calibration for the case of with and without ACET actuation of glucose, choline and H_2O_2. B) Comparison of the corresponding amperometric sensors' sensitivities for the cases of with and without ACET actuation (error bars indicate standard error). c) Comparison of the corresponding amperometric sensors' response time for the cases of with and without ACET actuation (error bars indicate standard error).

The representative results indicate that, across all three sensors, the activation of the ACET electrodes results in the enhancement of the sensor response in terms of both the output current level and sensitivity (defined as the slope of output current *vs.* analyte concentration). Furthermore, the results from the comparison of the amperometric sensor responses for the cases of with and without ACET actuation indicate that the sensor response time is reduced when activating the ACET electrodes. Our collective results, as illustrated in Fig. 6.9b, c , show that on average about 31.6% improvement in the sensitivity and 31.8% reduction in response time are achieved (repeated three times for each case, across all three sensing interfaces). The enhancement in the sensor

response can be attributed to both the effect of mixing (overcoming diffusion) as well as local temperature increment (*e.g.*, enhanced reaction rate at the sensor surface).

To validate the fully integrated system functionality, we demonstrated the elevation of sweat glucose after glucose intake in fasting subjects using actuation-assisted glucose sensor. Accordingly, standard iontophoresis protocol [48] was followed for sweat stimulation of three healthy subjects during 12-h fasting and 0.5 h after consumption of 30 g of glucose. Upon each stimulation, the secreted sweat sample was interfaced with the compartmentalized ACET actuation-assisted glucose sensor (worn on body). As shown in Fig. 6.10, the calibrated sweat sensor responses (measured in the presence of the ACET actuation, 3.5 V_{RMS}) for all three subjects indicate the elevation of glucose level in sweat upon glucose intake, reflecting the elevation of glucose in blood.

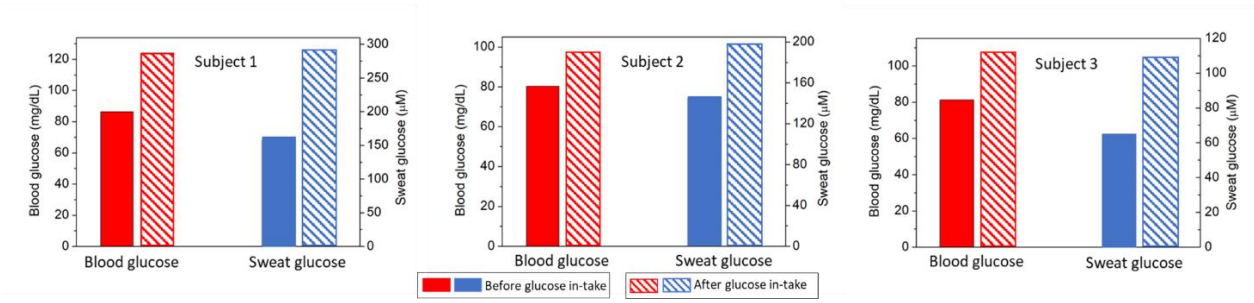

Figure 6.10: Comparison of blood and sweat glucose levels of three subjects during 12-h fasting and 0.5 h after glucose intake (30 g glucose).

In our efforts and as shown in Fig. 6.11a, we additionally validated our sensor's functionality by comparing the estimated glucose concentrations by our sensor *vs.* a gold standard instrument (YSI 2900D Biochemistry Analyzer, Xylem). Furthermore, as shown in Fig. 6.11b, we validated that valving and ACET actuation operations do not affect the glucose content of the introduced samples.

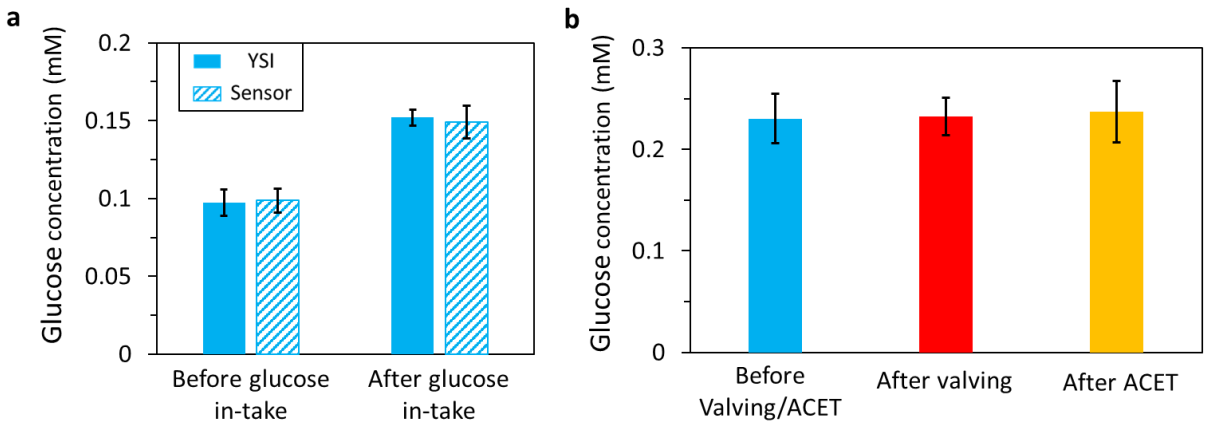

Figure 6.11: a) Comparison of the estimated glucose levels in two iontophoretically-induced sweat samples of a subject, as measured by the amperometric glucose sensor vs. YSI 2900D Biochemistry Analyzer (sample 1: during 12-h fasting, sample 2: 0.5 h after glucose intake, each sample was aliquoted and measured three times, error bars indicate standard error). b) Comparison of the measured glucose concentration (by YSI 2900D Biochemistry Analyzer) of a glucose-spiked PBS solution before and after valving/ACET actuation (duration of operation: 5 min, repeated three times for each case, error bars indicate standard error).

Chapter 7 Discussion and outlook

7.1 Discussion

The presented platform addresses the unmet need of active biofluid management for autonomous lab-on-the-body applications by devising and integrating compartmentalized biofluid actuation and biomarker sensing arrays within 3D wearable microfluidic systems. The platform overcomes the limitations of previously reported wearable devices in terms of lack of active biofluid handling and 2D spatial constraints, which in turn limited the diversity of sensing operations. The actuation array delivers a diverse set of operations including ACET actuation, valving, and reagent delivery, which can be integrated with electrochemical sensing interfaces. These operations are electronically programmable, practically rendering them tunable, addressable, and scalable. Accordingly, they can be utilized to implement versatile lab-on-the-body platforms for point-of-person monitoring.

Wearable ACET actuation is demonstrated to tunably induce biofluid motion with desired profiles, which can be adapted to deliver various biofluid manipulation functionalities. Specifically, here, asymmetric electrode configurations are used to induce microscale pumping on the order of 250 μm/s, which facilitates efficient and relatively long range (mm-scale) transport of species on the order of a few seconds. An array of rotationally symmetric electrode pairs is used to induce mixing. The effect of locally generated flow vortices (as induced by these electrodes) is characterized against advection-driven flow profiles. The results indicate that full mixing can be achieved in presence of relatively high advection flows, with flow rates that are three orders of magnitude higher than physiologically relevant flow rates (*e.g.*, as compared to sweat secretion rate for a 1 cm^2 stimulated area). The characterization results for both cases of pumping and mixing are strongly in agreement with the trends predicted by the ACET theory and our COMSOL simulation.

The wearable ACET-based biofluid actuation methodology is validated through on-body testing. This methodology can be extended to induce various other flow profiles through changing the electrode configuration and excitation settings. For example, with the aid of a symmetric and parallel coplanar electrode pair, out-of-plane mixing can be achieved, which as shown by Meinhart *et al.* (in the context of lab on a chip devices) can increase the analyte binding to the transducer's surface [50, 51].

Furthermore, reversible and repeatable multi-valving operations are demonstrated in serial and parallel configurations. These valving configurations can form the building blocks of multi-step and multi-chamber operations for large-scale and complex biofluid sample processing. To adapt the valving capability for sampling, routing, and compartmentalizing sweat, directly harvested from secreting glands, a pressure release mechanism was devised. To this end, an analogous electrical circuit explanation was used to model the sweat gland-microfluidic channel interface. This model provided the basis for the devised pressure release mechanism, which utilizes a secondary fluid pathway to eliminate pressure built-up across the glands or the valve breakage caused by the high pressure secreted sweat. Similar to the ACET mixing case, our results indicate that with the devised pressure release mechanism and valve design, robust biofluid compartmentalization can be achieved to manage high flow rates that are three orders of magnitude larger than sweat secretion rates.

The integration of the demonstrated biofluid actuation interfaces allows for the creation of new degrees of freedom for performing biomarker sensing-related operations in an autonomous fashion. The example enabling operations include temporal sampling, multi-on-demand biomarker sensing, and enhancement of sensor performance.

An illustrative programmable multi-compartment configuration was demonstrated that allows for time-sequential (temporal) sweat sampling at desired time-points, while addressing contamination challenges. Autonomous temporal sweat sampling was used to collect time-stamped sweat samples in order to characterize sweat glucose excursion in relation to blood glucose (upon glucose intake). Equivalently, this capability could be applied to obtain periodic and diurnal measures of biomarkers.

The multi-compartment configuration was combined with the demonstrated ACET actuation capability to perform multi-on-demand sensing with enhanced sensor performance. In that regard, we leveraged the devised vertical assembly approach to create sandwiched-like actuation/sensing interfaces, capable of simultaneously actuating and analyzing fluid. The results from the characterization of glucose, choline and H_2O_2 amperometric sensing interfaces indicate average improvement of about 31.6% in sensitivity and average reduction of 31.8% in response time. Characterizing H_2O_2 sensing interface was motivated by the fact that H_2O_2 conversion is the last reaction step involved in a large group of enzymatic sensing mechanisms (specifically, oxidase-based). Given that the improvement of the sensitivity and reduction of response time in both glucose and choline cases were on the same order of magnitude as that for the case of H_2O_2, one may speculate that the acceleration of the H_2O_2 conversion rate and/or enhanced diffusion by ACET actuation plays a significant role in the sensor performance enhancement.

To validate our technology in clinical settings, our wearable ACET actuation-assisted glucose sensor was incorporated in human subject testing experiments to demonstrate the elevation of the sweat glucose upon glucose intake. Additionally, the cortisol aptasensor was used to analyze the saliva samples obtained from four participants in TSST, which is a widely adopted social-evaluative stressor. Our sensor readouts successfully tracked the distinct elevation/recovery pattern

of salivary cortisol response in all four subjects (the measured trends were validated with LC-MS/MS, as a gold standard instrument).

7.2 Outlook

The complex 3D microfluidic architecture is realized through alignment of flexible adhesive tapes and plastic layers which are patterned with microfluidic embodiments and functional electrodes. As such, the spatial efficiency achieved through this 3D integration approach allows for the incorporation of a multitude of actuation and sensing operations. The inherent simplicity of the flexible device fabrication process sets forth a feasible path for scalable and low-cost manufacturing, which is critical at the prototyping level, for fueling large-scale clinical investigations, as well as the production level for commercialized consumer applications.

Future efforts will focus on the integration of additional electrochemical/physical sensors and parallelized biofluid processing units for calibrated (*e.g.*, temperature and pH), multiplex and periodic biomarker analysis. Wearable iontophoresis [11] and reverse iontophoresis [52] interfaces will be integrated for diurnal sampling and analysis of sweat and interstitial fluid. In that regard, the demonstrated *in-situ* co-factor agent and transduction mediator delivery methodology will be coupled with sensor surface optimization strategies (*e.g.*, in terms of probe density and non-specific bindings/adsorption) to devise wearable sweat and interstitial-fluid based sample processing and analysis. These efforts converge toward evaluating the device robustness in the context of daily routine activities as well as characterizing diurnal and longitudinal profiles of a panel of putative biomarkers to establish their clinical utility.

Altogether, the presented methodologies enable efficient, scalable, highly automated and complex biofluid processing and analysis operations. Accordingly, we expect this work to open new directions for wearable and microfluidic biomarker analysis by enabling advanced functionalities

such as periodic/continuous monitoring, sample processing/purification, and low-concentration (pM-level) analyte detection (fundamentally constrained by mass-transport limitations).

Broadly, the versatility of the methodologies allows for their integration, with minimal effort and reconfiguration, in other classes of biofluid analysis platforms, such as mobile and portable biosensors to analyze other sources of biomarkers such as blood and urine. The outcome will be an ecosystem of biomarker monitoring platforms that provide a comprehensive view of the body's dynamic chemistry at the point-of-person, thus enabling personalized and precision medicine.

References

1. Zhu, C. *et al.* Stretchable temperature-sensing circuits with strain suppression based on carbon nanotube transistors. *Nature Electronics* 1, 183–190 (2018).
2. Heikenfeld, J. *et al.* Wearable sensors: modalities, challenges, and prospects. *Lab Chip* 18, 217–248 (2018).
3. Chou, H.-H. *et al.* A chameleon-inspired stretchable electronic skin with interactive colour changing controlled by tactile sensing. *Nat. Commun.* 6, 8011 (2015).
4. Chen, X. *et al.* CVD-grown monolayer MoS2 in bioabsorbable electronics and biosensors. *Nat. Commun.* 9, (2018).
5. Han, S. *et al.* Battery-free, wireless sensors for full-body pressure and temperature mapping. *Sci. Transl. Med.* 10, (2018).
6. Lee, J. *et al.* Conductive fiber-based ultrasensitive textile pressure sensor for wearable electronics. *Adv. Mater.* 27, 2433–2439 (2015).
7. Dagdeviren, C. *et al.* Conformal piezoelectric systems for clinical and experimental characterization of soft tissue biomechanics. *Nat. Mater.* 14, 728–736 (2015).
8. Yokota, T. *et al.* Ultraflexible organic photonic skin. *Sci Adv* 2, e1501856 (2016).
9. Lochner, C. M., Khan, Y., Pierre, A. & Arias, A. C. All-organic optoelectronic sensor for pulse oximetry. *Nat. Commun.* 5, 5745 (2014).
10. Wang, C. *et al.* Monitoring of the central blood pressure waveform via a conformal ultrasonic device. *Nature Biomedical Engineering* 2, 687–695 (2018).
11. Emaminejad, S. *et al.* Autonomous sweat extraction and analysis applied to cystic fibrosis and glucose monitoring using a fully integrated wearable platform. *Proc. Natl. Acad. Sci. U. S. A.* 114, 4625–4630 (2017).

12. Kim, J., Campbell, A. S., de Ávila, B. E.-F. & Wang, J. Wearable biosensors for healthcare monitoring. Nat. Biotechnol. (2019). doi:10.1038/s41587-019-0045-y
13. Kim, J., Campbell, A. S. & Wang, J. Wearable non-invasive epidermal glucose sensors: A review. *Talanta* 177, 163–170 (2018).
14. Sempionatto, J. R. *et al.* Eyeglasses based wireless electrolyte and metabolite sensor platform. *Lab Chip* 17, 1834–1842 (2017).
15. Heikenfeld, J. Non-invasive Analyte Access and Sensing through Eccrine Sweat: Challenges and Outlook circa 2016. *Electroanalysis* 28, 1242–1249 (2016).
16. Glennon, T. *et al.* 'SWEATCH': A Wearable Platform for Harvesting and Analysing Sweat Sodium Content. *Electroanalysis* 28, 1283–1289 (2016).
17. Heikenfeld, J. *et al.* Accessing analytes in biofluids for peripheral biochemical monitoring. *Nat. Biotechnol.* (2019). doi:10.1038/s41587-019-0040-3
18. Durdiaková, J., Fábryová, H., Koborová, I., Ostatníková, D. & Celec, P. The effects of saliva collection, handling and storage on salivary testosterone measurement. *Steroids* 78, 1325–1331 (2013).
19. Mohamed, R., Campbell, J.-L., Cooper-White, J., Dimeski, G. & Punyadeera, C. The impact of saliva collection and processing methods on CRP, IgE, and Myoglobin immunoassays. *Clin. Transl. Med.* 1, 19 (2012).
20. Gao, W. *et al.* Fully integrated wearable sensor arrays for multiplexed in situ perspiration analysis. *Nature* 529, 509–514 (2016).
21. Lee, H. *et al.* Wearable/disposable sweat-based glucose monitoring device with multistage transdermal drug delivery module. *Sci Adv* 3, e1601314 (2017).

22. Hong, Y. J. *et al.* Blood Sugar Monitoring: Multifunctional Wearable System that Integrates Sweat-Based Sensing and Vital-Sign Monitoring to Estimate Pre-/Post-Exercise Glucose Levels (Adv. Funct. Mater. 47/2018). *Adv. Funct. Mater.* 28, 1870336 (2018).
23. Koh, A. *et al.* A soft, wearable microfluidic device for the capture, storage, and colorimetric sensing of sweat. *Sci. Transl. Med.* 8, 366ra165 (2016).
24. Sempionatto, J. R. *et al.* Skin-Worn Soft Microfluidic Potentiometric Detection System. *Electroanalysis* (2018). doi:10.1002/elan.201800414
25. Nyein, H. Y. Y. *et al.* A Wearable Microfluidic Sensing Patch for Dynamic Sweat Secretion Analysis. *ACS Sens* 3, 944–952 (2018).
26. Lu, Y. *et al.* AC Electrokinetics of Physiological Fluids for Biomedical Applications. *J. Lab. Autom.* 20, 611–620 (2015).
27. Chang, C.-C. & Yang, R.-J. Electrokinetic mixing in microfluidic systems. *Microfluid. Nanofluidics* 3, 501–525 (2007).
28. Nguyen, N.-T. & Wu, Z. Micromixers—a review. *J. Micromech. Microeng.* 15, R1–R16 (2004).
29. Suh, Y. K. & Kang, S. A Review on Mixing in Microfluidics. *Micromachines* 1, 82–111 (2010).
30. Stroock, A. D. *et al.* Chaotic mixer for microchannels. *Science* 295, 647–651 (2002).
31. Wu, H.-Y. & Liu, C.-H. A novel electrokinetic micromixer. *Sens. Actuators A Phys.* 118, 107–115 (2005).

32. Huang, S.-H., Wang, S.-K., Khoo, H. S. & Tseng, F.-G. AC electroosmotic generated in-plane microvortices for stationary or continuous fluid mixing. *Sens. Actuators B Chem.* 125, 326–336 (2007).
33. Wu, J., Lian, M. & Yang, K. Micropumping of biofluids by alternating current electrothermal effects. *Appl. Phys. Lett.* 90, 234103 (2007).
34. Du, E. & Manoochehri, S. Enhanced ac electrothermal fluidic pumping in microgrooved channels. *J. Appl. Phys.* 104, 064902 (2008).
35. Loire, S., Kauffmann, P., Mezić, I. & Meinhart, C. D. A theoretical and experimental study of ac electrothermal flows. *J. Phys. D Appl. Phys.* 45, 185301 (2012).
36. Wong, P. K., Wang, T.-H., Deval, J. H. & Ho, C.-M. Electrokinetics in Micro Devices for Biotechnology Applications. *IEEE/ASME Trans. Mechatron.* 9, 366–376 (2004).
37. Sin, M. L. Y., Gau, V., Liao, J. C. & Wong, P. K. Electrothermal Fluid Manipulation of High-Conductivity Samples for Laboratory Automation Applications. *JALA Charlottesv. Va* 15, 426–432 (2010).
38. González, A., Ramos, A., Morgan, H., Green, N. G. & Castellanos, A. Electrothermal flows generated by alternating and rotating electric fields in microsystems. *J. Fluid Mech.* 564, 415 (2006).
39. Hodgman, C. D. & Lind, S. C. Handbook of Chemistry and Physics. *J. Phys. Colloid Chem.* 53, 1139–1139 (1949).
40. Xia, L.-W., Ju, X.-J., Liu, J.-J., Xie, R. & Chu, L.-Y. Responsive hydrogels with poly(N-isopropylacrylamide-co-acrylic acid) colloidal spheres as building blocks. *J. Colloid Interface Sci.* 349, 106–113 (2010).

41. Harmon, M. E., Tang, M. & Frank, C. W. A microfluidic actuator based on thermoresponsive hydrogels. *Polymer* 44, 4547–4556 (2003).
42. Kim, Y. S. *et al.* Thermoresponsive actuation enabled by permittivity switching in an electrostatically anisotropic hydrogel. *Nat. Mater.* 14, 1002–1007 (2015).
43. Dong, L., Agarwal, A. K., Beebe, D. J. & Jiang, H. Variable-Focus Liquid Microlenses and Microlens Arrays Actuated by Thermoresponsive Hydrogels. *Adv. Mater.* 19, 401–405 (2007).
44. Wang, J. *et al.* Self-actuated, thermo-responsive hydrogel valves for lab on a chip. *Biomed. Microdevices* 7, 313–322 (2005).
45. Sonner, Z. *et al.* The microfluidics of the eccrine sweat gland, including biomarker partitioning, transport, and biosensing implications. *Biomicrofluidics* 9, 031301 (2015).
46. Moyer, J., Wilson, D., Finkelshtein, I., Wong, B. & Potts, R. Correlation between sweat glucose and blood glucose in subjects with diabetes. *Diabetes Technol. Ther.* 14, 398–402 (2012).
47. Bariya, M., Nyein, H. Y. Y. & Javey, A. Wearable sweat sensors. *Nature Electronics* 1, 160–171 (2018).
48. LeGrys, V. et al. Sweat Testing: Sample Collection and Quantitative Chloride Analysis: Approved Guideline, Third Edition2009. CLSI document C34-A3
49. Baronas, R., Ivanauskas, F. & Kulys, J. The Influence of the Enzyme Membrane Thickness on the Response of Amperometric Biosensors. *Sensors* 3, 248–262 (2003).
50. Sigurdson, M., Wang, D. & Meinhart, C. D. Electrothermal stirring for heterogeneous immunoassays. Lab Chip 5, 1366–1373 (2005).

51. Feldman, H. C., Sigurdson, M. & Meinhart, C. D. AC electrothermal enhancement of heterogeneous assays in microfluidics. *Lab Chip* 7, 1553–1559 (2007).
52. Bandodkar, A. J. *et al.* Tattoo-based noninvasive glucose monitoring: a proof-of-concept study. *Anal. Chem.* 87, 394–398 (2015).